PIEZO-ON-SILICON MICROELECTROMECHANICAL RESONATORS

A Thesis
Presented to
The Academic Faculty

By

Shweta Humad

In Partial Fulfillment
Of the Requirements for the Degree
Master of Science in the
School of Electrical and Computer Engineering

Georgia Institute of Technology
July 2004

PIEZO-ON-SILICON MICROELECTROMECHANICAL RESONATORS

Approved by:

Dr. Farrokh Ayazi, Advisor

Dr. Mark Allen

Dr. Oliver Brand

July 12, 2004

ACKNOWLEDGEMENTS

I would like to express my deepest appreciation to my thesis advisor and mentor, Dr. Farrokh Ayazi. He has provided me with constant support, encouragement, and opportunity. I would also like to thank the committee members, Dr. Mark Allen and Dr. Oliver Brand for their support. I want to acknowledge my colleagues in the NMASP group, Gavin Ho, Reza Abdolvand and Siavash Pourkamali for their help and the many useful discussions. I especially want to thank Gavin for all his help with ANSYS and modeling. I would also like to acknowledge all of my other colleagues in the IMEMS group for their assistance and friendship. The MiRC cleanroom staff at the Georgia Institute of Technology has been very helpful with special mention to Gary Spinner, Charlie Suh, Brandon Harrington and Vinny Nguyen. They have gone out of their way many a times to bring equipment up for me. Finally, I wish to thank my family, especially my father, mother, and brother for their continued moral support.

TABLE OF CONTENTS

LIST OF TABLES

LIST OF FIGURES

SUMMARY

This thesis reports on the use of sputter-deposited zinc-oxide as a transduction mechanism to actuate and sense single crystal silicon (SCS) microelectromechanical (MEMS) resonators. Low frequency prototypes of piezo-on-silicon resonators with operating frequencies in the range of hundreds of kHz were implemented using micromechanical single crystal silicon clamped-clamped beam resonators. The resonators reported here extend the frequency of this technology into very high frequency (VHF range) by using in-plane length extensional bulk resonant modes. This thesis outlines the design, implementation and characterization of high-frequency single crystal silicon (SCS) block resonators with piezoelectric electromechanical transducers. The resonators are fabricated on 4μm thick SOI substrates and use sputtered ZnO as the piezoelectric material. The centrally supported block resonators operate in their first and higher order length extensional bulk modes with high quality factor (Q). Measurement results are in good agreement with the developed ANSYS simulations.

CHAPTER I

INTRODUCTION AND MOTIVATION

Advanced consumer electronics pose severe limitations on the size and cost of the frequency selective units contained therein. Ongoing research activities in micro-electro-mechanical (MEMS) resonator technology have led to the miniaturization of these components. MEMS on a broad level can be defined as the integration of mechanical elements, sensors, actuators and electronics on a common substrate through microfabrication technology. The micromechanical components are fabricated using micromachining processes. Resonators are physical structures that have mechanical resonances occurring at specific frequencies. The shape and frequency of the resonator is dependant on the clamping conditions, effective mass (M_{eff}) and stiffness of the resonator (K_{eff}):

$$\omega_{resonance} = 2\pi f_{resonance} = \sqrt{\frac{K_{eff}}{M_{eff}}} \qquad [1.1]$$

The emerging technology of MEMS has made the miniaturization of resonators a reality, producing silicon based microelectromechanical resonators (MEMresonators) with high quality factors and Gigahertz resonant frequencies. MEMresonators are comprised of a microscale mechanical element and integrated transducers that convert the motion of the micromechanical element into electrical signal and vice versa. Various electromechanical transduction mechanisms such as electrostatic [1], magnetostrictive [2], piezoelectric [3] and thermal [4] have been developed. Capacitive and piezoelectric methods are preferred

because their transduction process is reversible (the element can be used for detection and actuation) and due to their ease of integration with CMOS circuitry.

Several all-silicon resonators with capacitive transduction mechanisms, schematically shown in figure 1.1 left, have been reported in the literature [1, 5-7], showing high mechanical quality factors and optimal performances in the IF and VHF range. A major drawback is the large motional resistance value of the capacitive resonators in the range of MΩ and its dependence on drive voltage [8]. The series motional resistance R_M plays a fundamental role when designing filters. In general, for both design and noise considerations, this resistance must be made as small as possible. On the contrary, piezoelectric resonators (figure 1.1 right) [2, 9-10] have smaller (kΩ and smaller) motional resistance and hence are more suitable for UHF applications. This advantage reduces the challenges that could be encountered in designing the sensing circuitry. In order to reduce the motional resistance of the capacitive resonators for higher frequency applications, sub-100nm capacitive gap spacing is needed, which complicates the fabrication process.

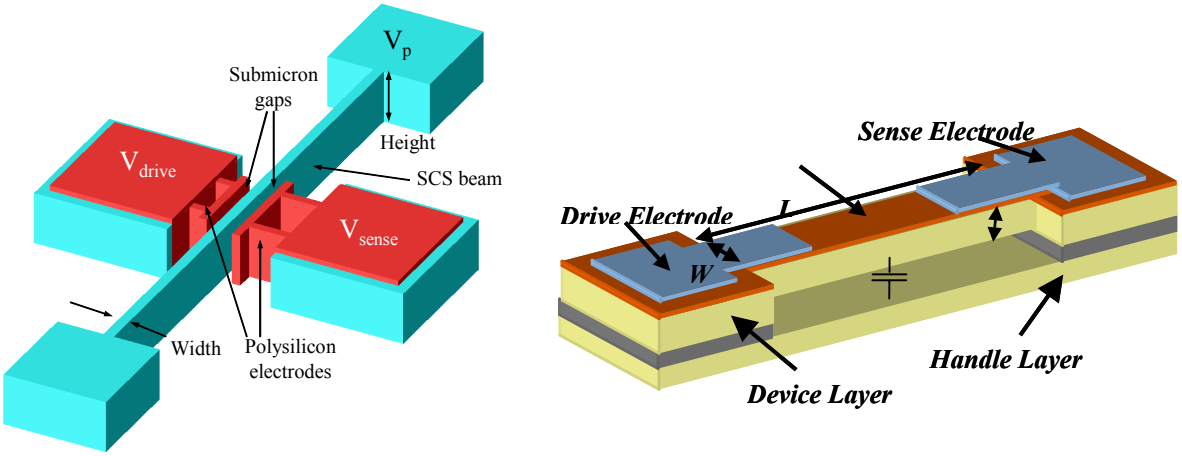

Figure 1.1 Schematic of a (left) clamped-clamped capacitive beam resonator; (right) a piezoelectrically actuated beam resonator

The electromechanical coupling factor is a coefficient related to the efficiency of the conversion process between electrical and mechanical phenomena. The input and output electromechanical coupling can be defined as:

$$\eta_{input} = \frac{F}{V} \text{ and } \eta_{output} = \frac{i}{x}$$

where F is the force generated due to the drive voltage V; and i is the output current as a result of the displacement x.

Let us compare the electromechanical coupling for the two transduction mechanisms by taking the example of a clamped-clamped beam resonator model. For a capacitive clamped-clamped beam its value is approximately equal to:

$$\eta_C = \frac{\partial C}{\partial x} V_p = \frac{\varepsilon_o A V_p}{d_d^2} \qquad [1.2]$$

where A is the electrode area, ε_o is the permittivity of the surrounding environment, V_P is the polarization voltage applied between the electrode and resonator, and d_d is the drive capacitive gap.

For a piezoelectric clamped-clamped beam resonator, η_P assumes the following value [11]:

$$\eta_P = 2.49 \cdot d_{31} E_P h_e \frac{b}{L} \qquad [1.3]$$

where d_{31} is the piezoelectric coefficient of the piezoelectric material, E_p the Young's modulus of the piezo material, h, b and L are the thickness, width and length of the beam respectively. The electromechanical coupling for the capacitive beam depends on the gap size, coupling capacitance as well as the DC bias voltage over the gap. It can be increased by reducing the gap size which is not an easy task, or by applying a large polarization voltage that requires larger DC supply voltages. On the other hand, the coupling can easily be increased for the piezoelectric resonator. This can be done by using materials having large piezoelectric coupling coefficients such as PZT and altering beam dimensions. The higher electromechanical coupling presented by the piezoelectric resonators allows using lower driving voltage for the same output current. Also there is no need for a polarization voltage V_p, therefore lowering the power requirements and the final system dimensions. The piezo-resonator can also perform better than the capacitive resonator at higher frequency, because its equivalent admittance is much higher and the signal output easier to be sensed. However, the quality factor (Q) values of the piezoelectric resonators are typically smaller than their capacitive counterparts.

A common disadvantage for both transduction mechanisms is the presence of non-linear phenomena. Electrical non-linearity stems from the general nonlinearity of a capacitive transducer as a function of the displacement from the equilibrium gap distance which has a major impact on the non-linearity present in the resonator response. This non-linearity

in the port capacitance can affect the trans-conductance spectrum of the resonator, showing spring softening, called Duffing behavior. This means that the frequency response shows hysteresis when the vibration amplitude becomes high enough. Non-linear Duffing behavior is also experimentally shown by the piezoelectric resonator for high input driving voltage (1.2 V_{p-p} for a 1.18 MHz resonator) [11]. Although this phenomenon cannot be linked to the admittance model, its explanation could be found in the approximations made in deriving the model itself. Above 5 V_{p-p}, the 0.5 μm-thick ZnO film shows electrical breakdown, resulting in permanent shorting. More recent studies of piezoelectric resonators realized with sol-gel-deposited PZT, showed a similar non-linear behavior, to which a frequency shifting probably induced by internal stress [12] in the SiO_2/Ta/Pt/PZT/Pt stack was added. The internal stress, acts on the equivalent spring constant of the resonator, shifting its resonance frequency. The level of stress seems to be theoretically unpredictable and needs to be experimentally determined for each batch.

The capacitive resonator is easily tuned through the polarization voltage. This allows for fine-tuning of the resonator center frequency. Because the resonant frequency of the piezo-resonator is set by its mechanical characteristics, the resonator needs to be "pulled" by external circuitry that could affect its external Q.

Coarse tuning of both types of resonators could be achieved by a post-processing mass addition. An interesting possibility to obtain coarse-tuning of piezoelectric resonators could be achieved by varying the polarization voltage applied during the film fabrication

process (sol-gel PZT). The applied electric field would slightly alter the piezoelectric properties, changing the resonance frequency of the whole structure. Tests relative to this coarse-tuning solution were reported in [13].

This thesis is organized into six chapters. A brief outline of the thesis is presented below. Chapter 1 provides an introduction to some actuation mechanisms, comparing capacitive with piezoelectric as the motivation behind the research entailed in this thesis. Chapter 2 is an overview of fundamental linear constitutive equations of piezoelectricity, and a brief literature review and summary of the various piezoelectric resonators. Chapter 3 introduces the bulk-mode piezo-on-silicon resonators. This chapter discusses their design, and modeling. Chapter 4 describes the piezo-on-silicon device fabrication process along with mask layout constraints. Chapter 5 presents the characterization results of the bulk-mode resonators, and provides discussion of these results. Finally, chapter 6 concludes the thesis and provides suggestions on future research direction.

CHAPTER II

REVIEW OF PIEZOELECTRIC RESONATORS

2.1. Introduction

Before we start the review of piezoelectric resonators it is instructive to introduce basic concepts related to the piezoelectric phenomenon and the zinc oxide material system. Piezoelectricity was first discovered in 1880 by Pierre and Jacques Curie. It provides the coupling between mechanical properties such as stress and strain and electrical properties of the crystal. Figure 2.1 shows schematically the general relationship between mechanical and electrical variables. Piezoelectric linear equations are coupled to the charge equations of electrostatics by means of piezoelectric constants. In a piezoelectric electromechanical resonator, the application of an alternating electric field to the electrodes of the resonator sets up a mechanical resonant mode.

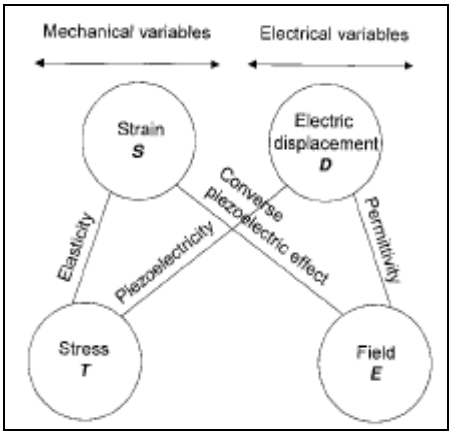

Figure 2.1 Relationship between mechanical and electrical variables

All crystal structures can be classified into one of 32 possible forms of crystal symmetry [14]. 11 of these forms are centrosymmetric. Of the remaining 21 non-centrosymmetric groups, 20 are known to be piezoelectric. In 10 of these crystal groups there is a permanent electric dipole, and the equilibrium of the electrostatic potential caused by this dipole can be distorted by mechanical stress (piezoelectricity) or by temperature change (pyroelectricity) For a material to exhibit piezoelectricity its crystal structure should have no center of symmetry, which means there is at least one axis in the crystal where the atomic arrangement appears different when proceeded in opposite directions along it. Although the piezoelectric phenomenon is non-linear, most applications utilize the operation conditions in which the piezoelectric response is nearly linear.

2.2. Linear constitutive equations of piezoelectricity

In piezoelectric materials, a stress T causes dielectric displacement D (charge Q per unit area) as a result of the direct piezoelectric effect shown in figure 2.2, given by,

$D = Q / A = dT$ (d expressed in coulombs/Newton) [2.1]

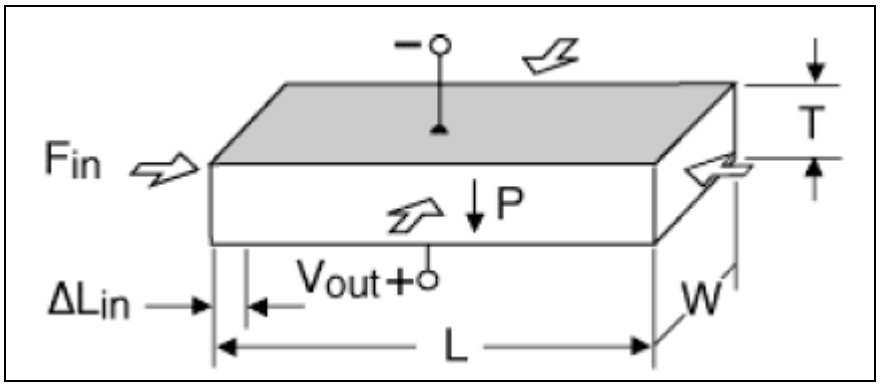

Figure 2.2 Schematic of direct piezoelectric effect

The converse effect shown in figure 2.3 is responsible for producing a strain *S* (Equation 2.2), when an electric field *E* is applied. The strain can be expansion or contraction depending on the polarity.

$S = dE$ (*d* expressed in meters/volt) [2.2]

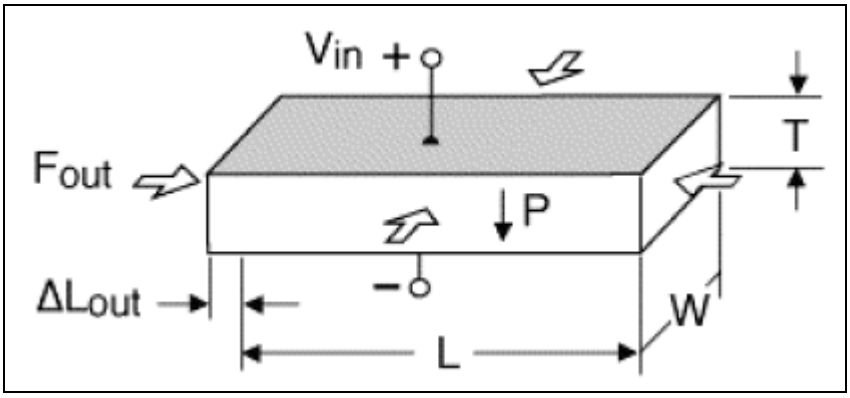

Figure 2.3 Schematic of inverse piezoelectric effect

For both the above equations [15], the proportionality constant is the piezoelectric constant *d*. The equations of state relating electric and elastic variables can be written in the "S-E" form:

$$T_i = C^E{}_{ij} S_j - e_{ij} E_j$$
$$D_i = e_{ij} S_j + \varepsilon^S{}_{ij} E_j$$

or alternatively in the "T-E" form:

$$S_i = s^E{}_{ij} T_j + d_{ij} E_j$$
$$D_i = d_{ij} T_j + \varepsilon^T{}_{ij} E_j$$

where the subscript indices take the values of $i, j = 1...6$. The matrices $c^E, s^E, e, d, \varepsilon^S, \varepsilon^T$, are the mechanical stiffness at constant electric field, the mechanical compliance at constant electric field, the stress piezoelectric coefficient, the strain piezoelectric coefficient, the permittivity at constant strain, and the permittivity at constant stress,

respectively. S and T are second order tensors and *d* is a third order tensor. Indices *ij* for *d* indicate the direction of the applied electric field and resultant strain respectively.

For ZnO the above equations take the form [16]:

$$\begin{pmatrix} T_1 \\ T_2 \\ T_3 \\ T_4 \\ T_5 \\ T_6 \end{pmatrix} := \begin{bmatrix} C_{11} & C_{12} & C_{13} & 0 & 0 & 0 \\ C_{21} & C_{22} & C_{23} & 0 & 0 & 0 \\ C_{31} & C_{32} & C_{33} & 0 & 0 & 0 \\ 0 & 0 & 0 & C_{44} & 0 & 0 \\ 0 & 0 & 0 & 0 & C_{44} & 0 \\ 0 & 0 & 0 & 0 & 0 & \frac{(C_{11} - C_{12})}{2} \end{bmatrix} \begin{pmatrix} S_1 \\ S_2 \\ S_3 \\ S_4 \\ S_5 \\ S_6 \end{pmatrix} - \begin{pmatrix} 0 & 0 & e_{31} \\ 0 & 0 & e_{31} \\ 0 & 0 & e_{33} \\ 0 & e_{15} & 0 \\ e_{15} & 0 & 0 \\ 0 & 0 & 0 \end{pmatrix} \begin{pmatrix} E_1 \\ E_2 \\ E_3 \end{pmatrix} \qquad [2.3]$$

$$\begin{pmatrix} D_1 \\ D_2 \\ D_3 \end{pmatrix} := \begin{pmatrix} 0 & 0 & 0 & 0 & e_{15} & 0 \\ 0 & 0 & 0 & e_{15} & 0 & 0 \\ e_{31} & e_{31} & e_{33} & 0 & 0 & 0 \end{pmatrix} \begin{pmatrix} S_1 \\ S_2 \\ S_3 \\ S_4 \\ S_5 \\ S_6 \end{pmatrix} + \begin{pmatrix} \varepsilon_{11} & 0 & 0 \\ 0 & \varepsilon_{11} & 0 \\ 0 & 0 & \varepsilon_{33} \end{pmatrix} \begin{pmatrix} E_1 \\ E_2 \\ E_3 \end{pmatrix} \qquad [2.4]$$

The e_{ij} are related to the d_{ij} through a tensor transformation involving elastic constants measured at constant electric field. The relationships are [16]:

$$d_{iJ} = \sum_K e_{iK} S^{\varepsilon}_{KJ}$$
$$e_{iJ} = \sum_K d_{iK} C^{\varepsilon}_{KJ} \qquad [2.5]$$

The d_{ij} coefficients can be found by inverting the C_{IJ} matrix to find S_{IJ} and then using equation 2.5:

In accordance with the assumed kinematics of the structure, the shear stress and shear strains are neglected ($S_4 = S_5 = S_6 = T_4 = T_5 = T_6 = 0$). The electrodes that cover the

piezoelectric layers of the structure are laid perpendicular to the vertical poling direction (z). The electric boundary conditions are applied using these electrodes, thus, only a vertical electric field E_3, may develop. Accordingly, the axial and lateral electric fields are neglected ($E_1 = E_2 = 0$). This is justified for a structure in which the thickness is small relative to the length and width dimensions. When the symmetry of a specific material's crystal structure and transformation operations are considered, many of the coefficients in the *e,* and *d* matrices are found to be related to each other or zero. Under these assumptions, the constitutive equations 2.3 and 2.4 of piezoelectricity are simplified and may be written in the compact form:

$$\begin{pmatrix} T_1 \\ T_2 \\ T_3 \end{pmatrix} = \begin{pmatrix} C_{11} & C_{12} & C_{13} \\ C_{12} & C_{11} & C_{13} \\ C_{13} & C_{13} & C_{33} \end{pmatrix} \begin{pmatrix} S_1 \\ S_2 \\ S_3 \end{pmatrix} - \begin{pmatrix} e_{31} \\ e_{31} \\ e_{33} \end{pmatrix} E_3$$

$$D_3 = \begin{pmatrix} e_{31} & e_{31} & e_{33} \end{pmatrix} \begin{pmatrix} S_1 \\ S_2 \\ S_3 \end{pmatrix} + \left(\varepsilon^{S}{}_{33}\right) E_3$$

While the piezoelectric matrices appear to be a second-order tensor, it must be remembered that it is still a third-order tensor.

2.3. Piezoelectric Zinc oxide

Zinc oxide (ZnO) is a hexagonal, wurtzite-type crystal [17] having a 6 mm symmetry. 'mm' is one of the Hermann-Mauguin symbols used to describe crystal classes from crystal symmetry content. It refers to the unique mirror planes existing in a crystal structure. The two important characteristics of the wurtzite structure are the noncentral

symmetry and polar surfaces. The structure of ZnO can be described as a number of alternating planes composed of tetrahedrally coordinated O^{2-} and Zn^{2+} ions, stacked alternately along the c-axis as shown in figure 2.4. The oppositely charged ions produce positively charged (0001)-Zn and negatively charged (0001)-O polar surfaces, resulting in a normal dipole moment and spontaneous polarization along the c-axis.

Piezoelectric transduction has been employed in various micromachined resonators using an extensive range of piezoelectric materials, summarized in table 2.1. The choice of material is determined by the specific requirements for elastic, piezoelectric, dielectric, fundamental fabrication constraints such as substrate-film adhesion, and etching selectivity to mention a few. For the current discussed in this thesis, ZnO was used for a number of reasons. ZnO offers a large piezoelectric coupling strength. Its sputtering process is a robust, well-characterized one that can be performed in-house. Also it allows for simple process integration, i.e. it can be deposited on many substrates without the need for complicated electrodes (e.g. Pt/TiO_2 or RuO_2 for PZT). ZnO films need no post-deposition poling treatment to align dipoles for preferred orientation. Finally post-CMOS integration of ZnO can be realized [18].

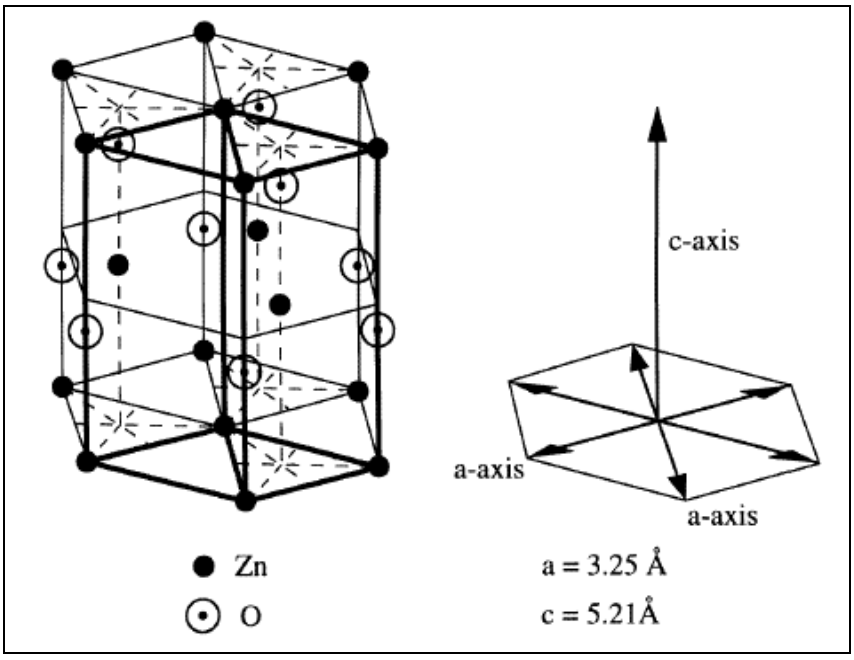

Figure 2.4 ZnO wurtzite crystal structure

Table 2.1 Properties of some piezoelectric materials

Material	Formula	Form	Piezoelectric constant (pm/V or pC/N)
Ammonium dihydrogen phosphate (ADP)	$NH_4H_2PO_4$	Single crystal	$d_{36} = 48$
Barium titanate	$BaTiO_3$	Single crystal	$d_{15} = 587$
Barium titanate	$BaTiO_3$	Polycrystalline ceramic	$d_{15} = 270$
Lead zirconate titanate (PZT)	$PbZr_{0.6}\ Ti_{0.40}O_3$	Polycrystalline ceramic	$d_{33} = 117$
Lead lanthanum zirconate titanate (PLZT)	$Pb_{0.925}La_{0.5}Zr_{0.56}Ti_{0.44}O_3$	Polycrystalline ceramic	$d_{33} = 545$
Polyvinylidene fluoride	$(CH_2CF_2)_n$	Oriented film	$d_{31} = 28$
Potassium dihydrogen phosphate (KDP)	KH_2PO_4	Single crystal	$d_{36} = 21$
Quartz	SiO_2	Single crystal	$d_{11} = 2.3$
Zinc oxide	ZnO	Single crystal	$d_{33} = 12$

2.4. Piezoelectric Resonators

Piezoelectric acoustic wave devices have been in commercial use for more than 60 years. The telecommunications industry is the largest consumer, accounting for ~3 billion acoustic wave filters annually, primarily in mobile cell phones and base stations. These are typically surface acoustic wave (SAW) devices, and act as band-pass filters in both the radio frequency and intermediate frequency sections of the transceiver electronics. Other applications include automotive applications (torque and tire pressure sensors), medical applications (chemical sensors), and industrial and commercial applications (vapor, humidity, temperature, and mass sensors). Acoustic wave sensors are competitively priced, inherently rugged, very sensitive, and intrinsically reliable.

Acoustic wave devices are described by the mode of wave propagation through or on a piezoelectric substrate. Acoustic waves are distinguished primarily by their velocities and displacement directions; many combinations are possible, depending on the material and boundary conditions. The various modes of wave propagation are briefly compared and described below.

2.4.1. Bulk Acoustic Wave Resonator

Bulk acoustic wave (BAW) resonators also called thickness shear mode (TSM) resonators have been used as quartz crystal microbalance (QCM) for a long time to monitor thin film deposition in vacuum or gas [19] and recently in the liquid phase as well [20, 21]. They typically consist of a thin disk of AT-cut quartz as the resonating body with circular electrodes patterned on both sides as shown in figure 2.5. On applying a varying voltage across the electrodes, the crystal undergoes a shear deformation, and a

BAW resonance occurs in this device due to coherent reflections at the top and bottom boundaries of the plate [22]. Considering the wave originating at the top electrode, its resonance condition can be determined by tracing its path. As it transitions the crystal it gets reflected (with phase shift $\phi = \pi$) at the bottom crystal face, and returns to the top again reflecting (with $\phi = \pi$) propagating downward with a total phase shift of $2kh_s + 2\phi$, h_s being the thickness of the crystal. When this total phase shift is an integer multiple of 2π, constructive interference between the incident and reflected wave leads to resonance given by [23],

$$\omega = \frac{2\pi v_S}{\lambda} = k \qquad [2.5]$$

where λ is acoustic wavelength and v is shear wave velocity. Resonance occurs when the crystal thickness is a multiple of half the acoustic wavelength.

The shear horizontal wave does not radiate appreciable energy into liquids, allowing liquid operation without excessive damping. Under vacuum, the rigid attachment of a film of mass Δm to the crystal surface causes a decrease Δf in the resonant frequency. The relationship between Δf and Δm is linear in the limit of small Δm was first derived by Sauerbrey [19], given by:

$$\frac{\Delta f}{f_o} = -\frac{\Delta m}{m} \qquad [2.6]$$

where f_o is the resonant frequency and m the mass of the unloaded resonator. The mass sensitivity of a 5 MHz quartz crystal is approximately 0.057 Hz cm^2 ng^{-1}. The frequency is given by, $f = \frac{Nv}{2h}$ [24] where h is the plate thickness, v the mode velocity, and N a positive integer representing harmonics of the fundamental frequency.

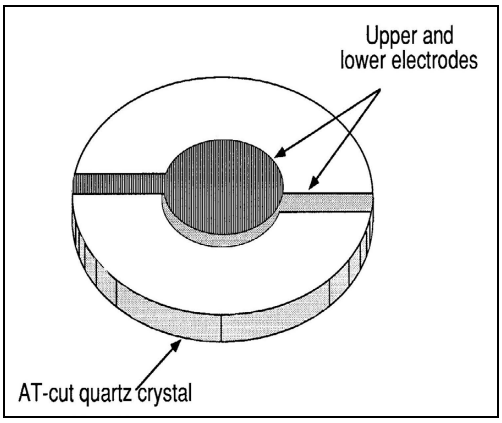

Figure 2.5 Schematic of a TSM quartz resonator

Typical TSM resonators operate between 5 and 30 MHz [25]. Making thin BAW devices, called film bulk acoustic resonators (FBARs) shown in figure 2.6, allows operation into the GHz range [26-30]. But thinning the resonators beyond the normal range results in fragile devices that are difficult to manufacture and handle. An FBAR employs a metal-piezo (eg. AlN) - metal sandwich. FBARs also provide increased mass sensitivity. The FBAR suffers from the fact that a large acoustic impedance mismatch must exist on both sides of the piezoelectric body. This requires incorporating a Bragg reflector on the bottom side of the piezoelectric (SMR- Solidly Mounted Resonator) or an air/crystal interface (FBAR) under the resonator. The Bragg reflector is made up of at least 3 to 4 pairs of acoustically dissimilar materials. If an air/crystal interface is required on both sides of the piezoelectric, the silicon needs to be etched from the back side. This technique has manufacturability issues and makes the supporting structure weak. Agilent Technologies avoids backside etch by forming shallow etch pits on the front side of the silicon surface which are back filled with oxide as shown in figure 2.7. The wafer is then polished down and further processed to deposit and pattern the metal and AlN. A final

release step is carried out to etch away the oxide from the pits. The piezo-on-silicon devices discussed in this thesis are fabricated directly on SOI wafers, and do not require a custom made starting wafer. Also it is critical to maintain a uniform thickness for FBAR devices for frequency control, where as this is not an issue for the longitudinal mode piezo-on-silicon devices, hence allowing multiple frequency resonators to be fabricated on-chip. FBAR will need various piezo film thicknesses on chip for the same and this will complicate the manufacturing process.

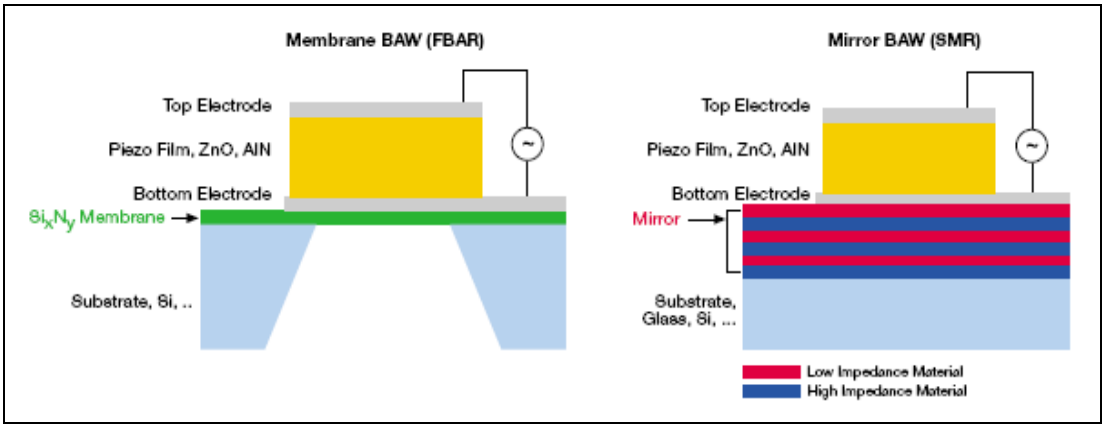

Figure 2.6 Schematic of a FBAR and a SMR

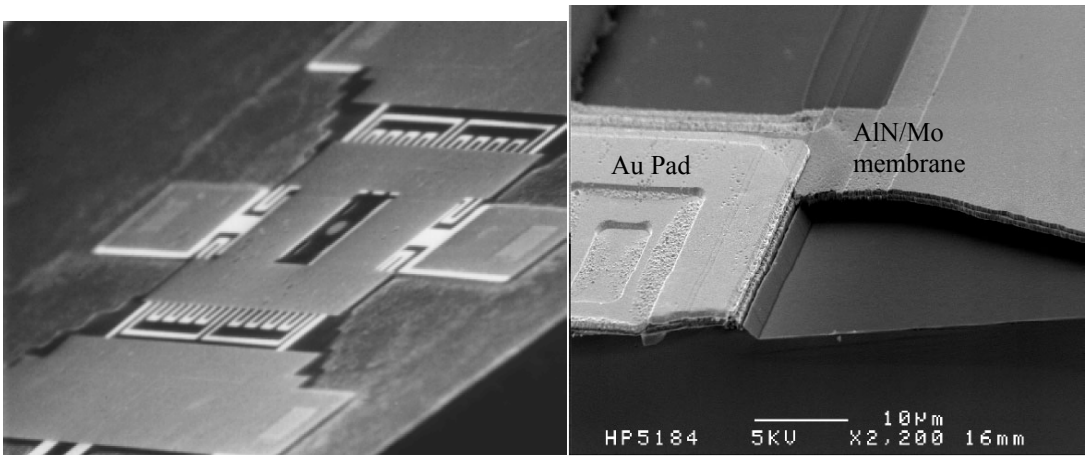

Figure 2.7 SEM of an 'Air Bridge' Agilent FBAR with meandering lines to tune the frequency with on-chip heaters (left); a portion of the membrane stretching over a micro-machined silicon pit (right)

2.4.2. Surface Acoustic Wave Resonator

The surface acoustic mode was discovered by Rayleigh in 1887. Propagation of the wave is confined to the stress free boundary of the surface of the crystal in these devices, also called surface-skimming waves. The frequencies of SAW resonators are usually between 50 MHz and a few GHz [31]. In order to satisfy the stress free boundary conditions, compressional and shear waves propagate together such that surface traction forces are zero. The amplitude of the SAW decays rapidly with distance into the bulk of the crystal. Majority of the strain energy is well within one wavelength of the surface. At higher frequencies, and i.e. shorter wavelengths, acoustic energy is confined more closely to the surface and wave sensitivity to surface perturbation increases.

Surface acoustic waves can be detected and excited by patterned inter-digitated transducers (IDT) shown in figure 2.8, on the surface of the piezoelectric crystal. Each 'finger' of the IDT is the origin of a SAW. The periodicity, that is the spacing *d* between the IDT fingers should match the wavelength of the SAW occurring at $f = v_P / d$ where v_P denotes the propagation velocity. Two port devices as shown in figure 2.9a have one IDT as a transmitter and another as a receiver. One port resonators seen in figure 2.9b consist of one IDT in between two reflectors. The resonant frequency is given by, $f_o = \frac{n v_P}{2l}$ where *l* is the distance between the reflectors.

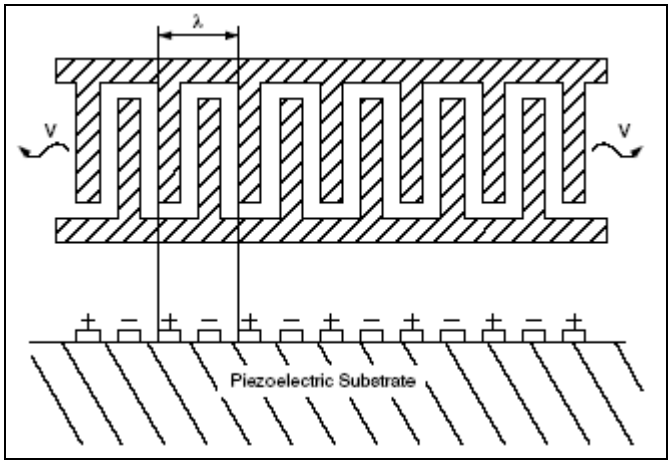

Figure 2.8 Schematic of a Inter-digital Transducer

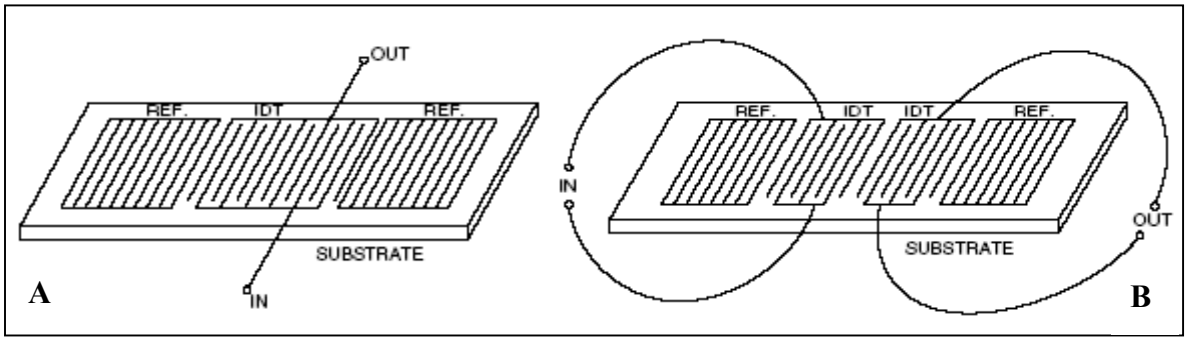

Figure 2.9 A) One-port SAW resonator; B) Two-port SAW resonator

Presence of surface-normal displacement components makes the device poorly suited for liquid sensing applications, because these components generate compressional waves in the liquid. The power thus dissipated causes attenuation of the SAW. These sensors have higher mass sensitivities than TSM but are not suitable in liquid media because of their high damping. The quality factor *Q* of SAW devices is between 6000 and 12000, which is considerably lower than that of TSM resonators operating in air (20000-50000 for a 10 MHz fundamental frequency). In spite of this, the relative ease of manufacturing SAWs, using one or two photoresist and metal deposition steps, has made them the technology of

choice. Surface waves have been extensively used for sensing chemical vapor [32-35], and for measuring force, acceleration, pressure [36, 37], as well as the properties of viscoelastic materials and liquids [38].

2.4.3. Flexural Plate Wave Resonator

Flexural Plate Wave (FPW) also called Lamb waves propagate in a thin membrane as shown in figure 2.10. The key sensing element in the FPW sensor is a thin plate along which flexural plate waves propagate [39]. The thickness of the plate is much smaller than the wavelength of the ultrasonic waves propagating in it, and therefore the wave propagates at a velocity that is lower than the speed of sound. The plate is so thin that its elastic response can be considerably influenced by in-plane tension that develops during the initial fabrication process. The mechanical and material properties of the membrane allow external forces and stress to alter the behavior of the device. Plate waves, unlike surface acoustic waves, have a phase velocity that depends on the thickness of the propagating medium.

The acoustic waves of a FPW are generated by the application of two sinusoidal signals 180° out of phase to the IDT. The period and orientation of the IDTs determines the wavelength and direction of the generated acoustic waves, respectively. The waves then propagate away from the IDTs, along the composite membrane, the thickness of which must be significantly smaller than the wavelength of the acoustic wave. The waves generated from one set of IDTs can be detected by another set of appropriately placed IDTs.

FPW devices are composed of four primary elements: an amorphous silicon nitride membrane, the supporting silicon structure, an active piezoelectric layer, and electrode layers including a ground plane and interdigitating transducers (IDTs) that sandwich the piezoelectric layer.

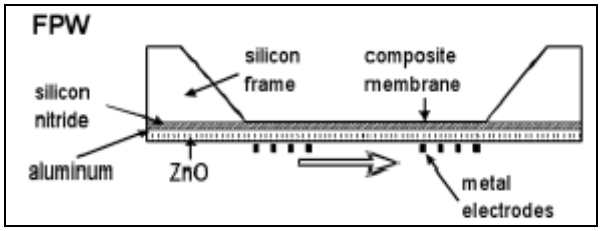

Figure 2.10 Schematic of a FPW

A unique feature of this device is that it can be dimensioned so that its phase velocity is lower than that of most liquids. When the FPW device comes in contact with a liquid, a slow mode of propagation exists in which there is no radiation from the plate. Thus the FPW device functions well in liquid environments. Another advantage of these devices is that the sensitive layer can be deposited on either side of the membrane. Deposition on the back side, i.e. the unprocessed side of the wafer enables isolation of the on-chip circuitry from the chemicals to be sensed [40, 41]. The frequencies employed in FPW devices are usually in the range of 1-10 MHz [42] which is much lower than those in SAW and APM sensors.

2.4.4. Acoustic Plate Wave Resonator

Acoustic devices operating in this mode utilize a shear horizontal (SH) acoustic plate mode, in which particle displacement is predominantly parallel to the device surface and normal to the direction of propagation as shown in figure 2.11. The operating frequencies

typically are greater than 100 MHz. Acoustic waveguides confine the energy between the upper and lower surfaces of the plate. As a result, both surfaces undergo displacement, so detection can occur on either side. This is an important advantage, as one side contains the IDTs that must be isolated from conducting fluids or gases, while the other side can be used as the sensor. As with the TSM resonator, the relative absence of a surface-normal component of wave displacement allows the sensor to come into contact with liquid for biosensor applications. Although these devices are more sensitive to mass loading than the TSM resonator, they are less sensitive than SAW sensors. This is mainly because the sensitivity to mass loading and other perturbations depends on the thickness of the substrate, with sensitivity increasing as the device is thinned. The minimum thickness is constrained by manufacturing processes. Also, the energy of the wave is not maximized at the surface, which reduces sensitivity.

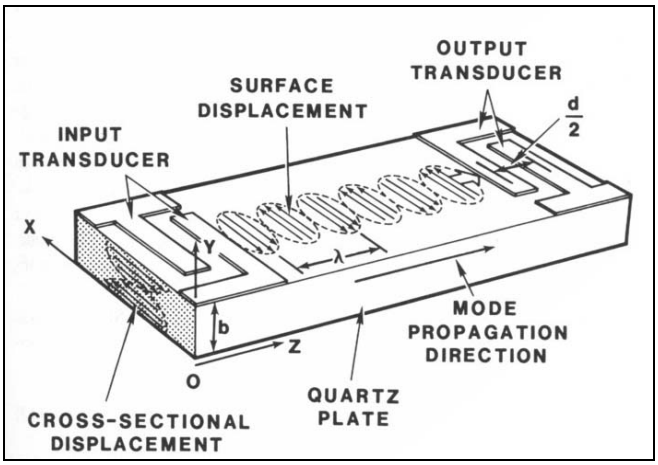

Figure 2.11 Schematic of an APM device showing SH displacement

CHAPTER III

BULK-MODE PIEZO-ON-SILICON RESONATORS

3.1. Introduction

Piezoelectric zinc oxide thin films are used as a transducer material in various mechanical sensors, acoustic wave devices, acoustic microscopy and acousto-optic devices. Piezoelectric actuation is advantageous because it decreases the insertion loss and avoids the need for a bias voltage. SCS was chosen as the resonator body because of its low temperature coefficient of frequency, stress free mechanical properties and it has higher inherent quality factor as compared to bulk piezoelectric. This chapter will provide an in depth discussion on the modeling and design of the piezoelectrically-actuated SCS block resonators.

3.2. Flexural-Mode Clamped-Clamped Beam Resonators

The first generation of the devices reported in this work were low-frequency flexural-mode clamped-clamped beam resonators ($f_{resonant}$<17MHz) operating in their out-of-plane flexural modes [43, 44]. Similar clamped-clamped resonant beams were previously demonstrated in [13] using SiO_2 as the resonating element, but low quality factors were reported. In addition, the frequency of the piezo-on-silicon resonators fabricated on SOI substrates is voltage-tunable.

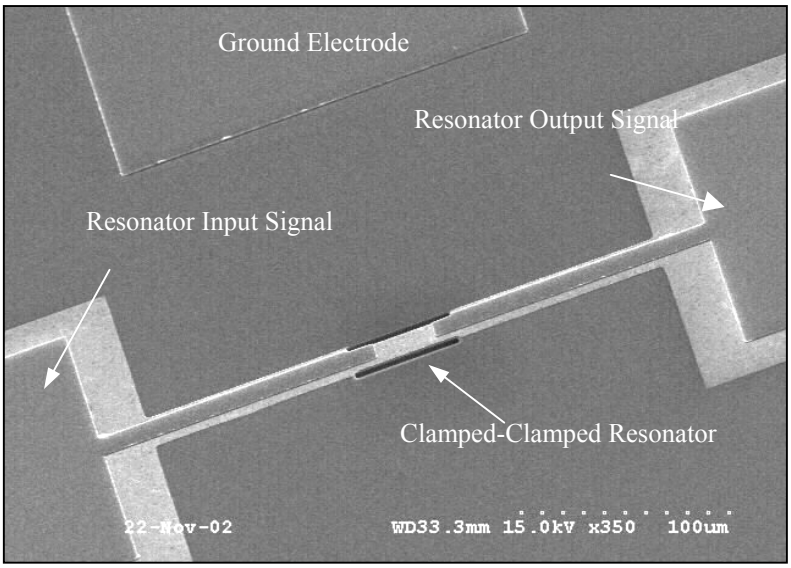

Figure 3.1 SEM view of a SCS piezoelectric beam resonator

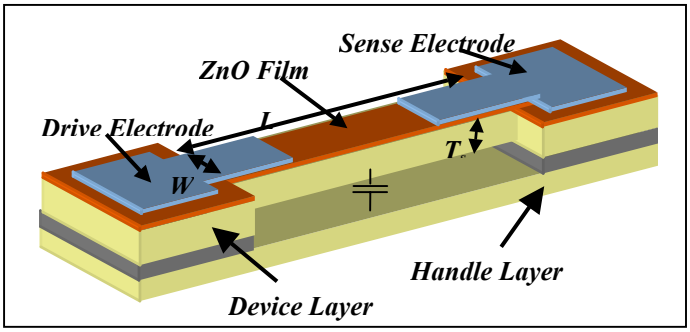

Figure 3.2 Schematic of the piezo-on-silicon beam resonator

When an AC voltage is applied to the drive electrode, the active piezoelectric film is producing a distributed moment, which causes the beam to deflect. Such a deformation is sensed by the piezoelectric material on the opposite side of the beam. The admittance modeling of a doubly-clamped piezoelectric beam resonator was taken into account during the design phase [11]. The electromechanical coupling coefficients at the input port η_{in} and at the output port η_{out} of the resonator, with the assumption that the thickness of the thin piezoelectric layer is negligible, are expressed by:

$$\eta_{in} = \frac{d_{31} E_p T_s}{2} \int_0^L W_i''(x)\Phi(x)dx \qquad \eta_{out} = -\frac{d_{31} E_p T_s}{2} \int_0^L W_o(x)\Phi''(x)dx \qquad [3.1]$$

where d_{31} is the transverse piezoelectric coefficient, E_p is the modulus of elasticity of zinc oxide, T_s is the thickness of the beam, $W(x)$ is the electrode width, and $\Phi(x)$ is the mode shape of the clamped-clamped beam. The equivalent motional resistance of the resonator depends on the squared inverse of the electromechanical coupling; therefore the values of η_{in} and η_{out} need to be maximized to achieve low values of the motional resistance.

The final input to output admittance Y_{oi} of the SCS resonator with piezoelectric transduction can be expressed as:

$$Y_{oi} = \frac{\left(2.49 \cdot d_{31} E_p T_s \frac{W}{L}\right)^2 s}{M_1 s^2 + \frac{M_1 \omega_n}{Q} s + K_1} \qquad [3.2]$$

where M_1 and K_1 are first mode equivalent mass and stiffness of the micromechanical resonator, ω_n is the natural resonance frequency of the beam, and s is the Laplace variable. If the thickness of the piezoelectric film is negligible compared to the resonator body, the first mode resonance frequency of the beam is set primarily by the SCS layer and can be approximated by:

$$f_o \approx 1.03 \frac{T_s}{L^2} \sqrt{\frac{E_s}{\rho_s}} \qquad [3.3]$$

where E_s and ρ_s are respectively the modulus of elasticity and the density of silicon.

The resonator reported in this thesis extends the frequency of this technology into very high frequency (VHF range) by using in-plane length extensional bulk resonant modes.

3.3. Bulk-Mode Block Resonators

The free-free beam configuration shown in figure 3.3 was initially investigated by William Newell [45] in 1970. Batch fabrication and miniaturization was not possible due to the lack of technology. The demonstrated dimensions were in the range of inches and a stainless steel body was implemented with 8 μm of cadmium sulphide as the piezoelectric layer.

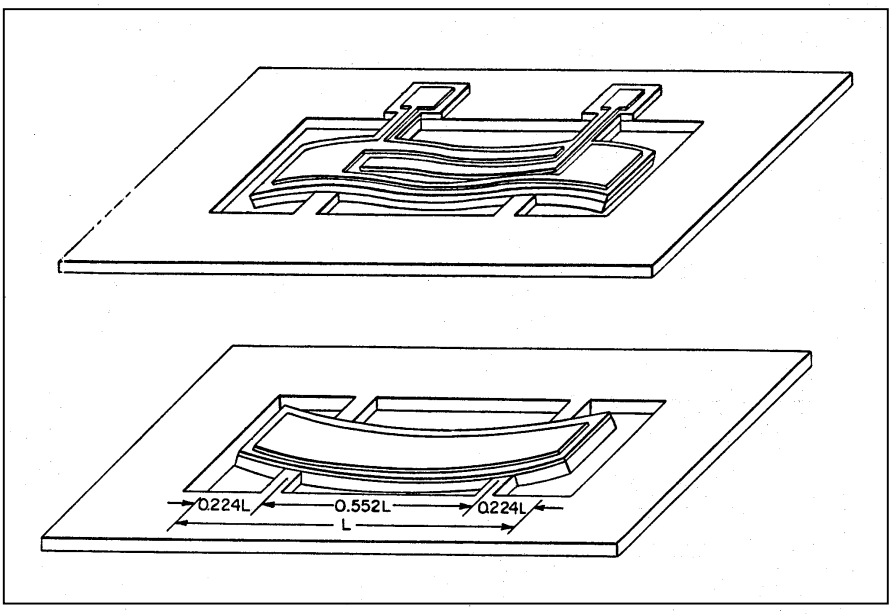

Figure 3.3 Newell configurations of free-free beam resonators from 1970

This thesis has realized the miniaturization of block resonators (similar to the free-free beams) operating in their bulk length extensional modes. The resonator is centrally supported by self aligned small tethers. Single crystal silicon is used as the resonating element because of its high inherent mechanical quality factor and stress free properties. Piezoelectric sense and actuation is provided by a thin ZnO film sputtered directly on silicon, sandwiched between the top aluminum electrodes and the bottom low resistivity SCS substrate. The ZnO film acts also as insulator between the top aluminum electrode

and bottom device layer. The elimination of the bottom metal electrode conventionally used in piezoelectric devices is introduced to reduce the number of stacked layers, which could ultimately increase the quality factor of the resonator.

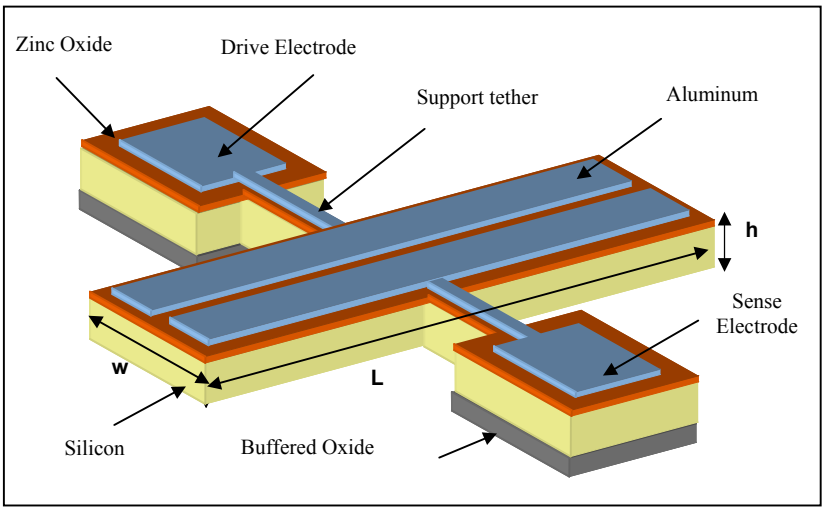

Figure 3.4 Schematic of the piezo-on-silicon block resonator

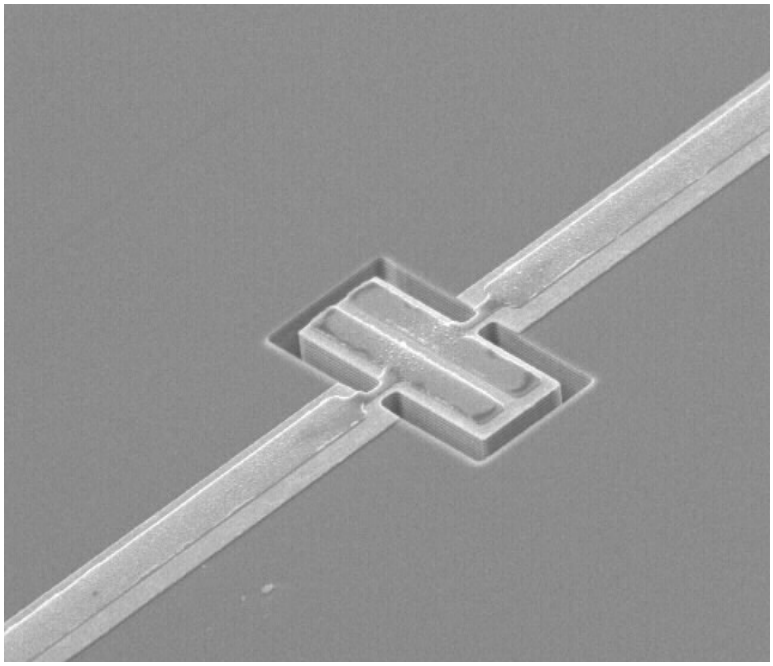

Figure 3.5 SEM picture of a fabricated 60μm×30μm piezo-on-silicon block resonators

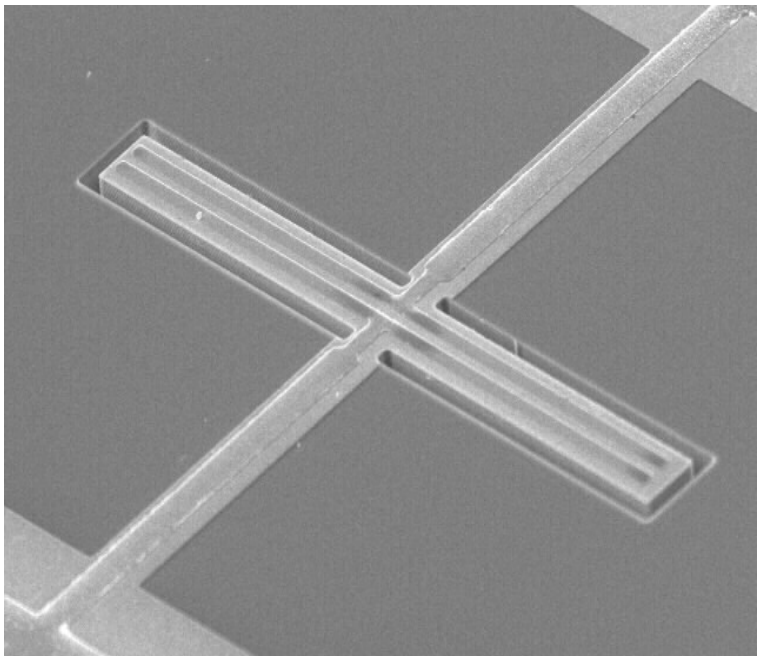

Figure 3.6 SEM pictures of a fabricated 240μm×20μm piezo-on-silicon block resonators

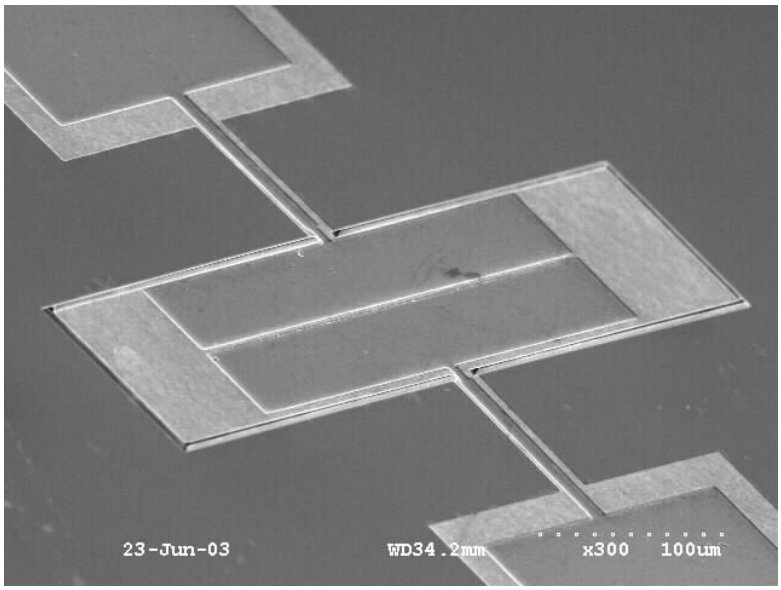

Figure 3.7 SEM pictures of a fabricated 480μm×120μm piezo-on-silicon block resonators

Design of support

The odd modes have a node at the center of the block (x = L/2). This is the ideal location to support the block. However, there is modal displacement at x = L/2 for the even modes. Although the even modes can be excited with the electrode configuration above, clamping them at the center will cause excessive support losses. For the odd modes, the resonating structure is coupled to the support via the lateral deformation at the support location. This lateral deformation couples the resonator to the surroundings and causes excessive clamping losses if not minimized.

The block resonators are more attractive than the beam resonators because they can be supported in the vicinity of nodal lines for the desired mode of operation unlike beams that have to be supported at either end.

3.3.1. Mode Shape and Natural Frequency

In general, the steady state solution for the response of a mechanical system can be expressed as:

$$Z(s,x,y,z) = \overline{Z}(s)u(x,y,z) \qquad [3.4]$$

where *u(x)* is the mode shape as shown in figure 3.9, and $\overline{Z}$ is the amplitude of vibration. The 1D mode shapes and natural frequencies of a free-free extensional block resonator are given by [46]:

$$\phi(x) = \cos\left(\frac{n\pi x}{L}\right) \text{ for } x = [0, L] \qquad [3.5]$$

$$\omega_n = \frac{n\pi}{L}\sqrt{\frac{E}{\rho}} \qquad [3.6]$$

where n is the mode number (n = 1,2,3,…), L is the length of the block, and E and ρ are the Young's modulus and density of the structural material (Si), respectively. The inverse piezoelectric effect can only be detected when the electrodes posses a net charge. Hence, even modes cannot be detected and a response is observed only for odd-numbered modes. Longitudinal modes have several advantages over flexural modes. For a device of a given dimension, higher resonant frequency can be obtained with longitudinal modes. Also the insertion losses are lower. Additionally the nodal support is less critical. In a free-free flexural device, twisting of the nodal supports contributes a spring constant that is comparable to that from the bending of the resonator itself. Therefore resonant frequency of the device will be influenced by the nodal support dimensions. However with longitudinal modes relatively wider central nodal supports can be used. Furthermore, the thickness is not critical for longitudinal mode of vibration. The frequency is determined almost entirely by length rather than both length and thickness for flexural resonators.

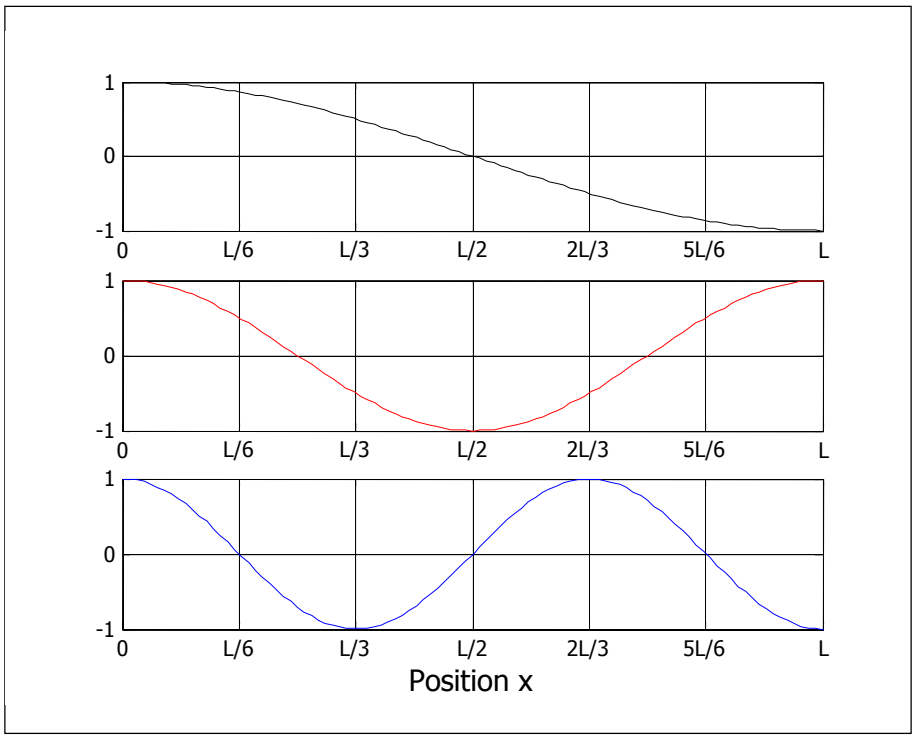

Figure 3.8 Modal Displacement for the first three length-extensional modes

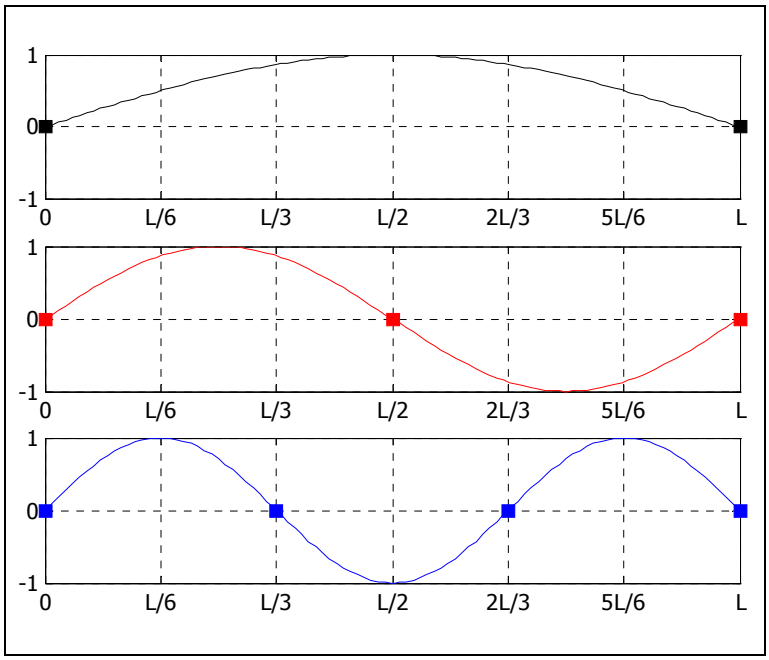

Figure 3.9 Strain for the first three length-extensional modes

3.3.2. Electromechanical Modeling

The admittance Y_{21} of a two-port resonator is defined as the ratio between the output current I_2 and the input voltage V_1 given by:

$$Y_{21}(s) = \frac{I_2(s)}{V_1(s)} \quad [3.7]$$

Equation 3.7 can also be expressed as:

$$\begin{aligned} Y_{21}(s) &= \left(\frac{F(s)}{V_1(s)}\right)\left(s\frac{Z(s)}{F(s)}\right)\left(\frac{1}{s}\frac{I_2(s)}{Z(s)}\right) \\ &= \eta_1(s)\cdot M(s)\cdot \eta_2(s) \end{aligned} \quad [3.8]$$

where η_1, η_2, and M are the input and output electromechanical coupling coefficients with units of N/V or C/m, and the mechanical mobility in m/(Ns), respectively.

$$\eta_1(s) = \frac{F(s)}{V_1(s)} \quad [3.9]$$

$$\eta_2(s) = \frac{1}{s}\frac{I_2(s)}{Z(s)} = \frac{Q_2(s)}{Z(s)} \quad [3.10]$$

$$M(s) = s\frac{Z(s)}{F(s)} \quad [3.11]$$

In order to determine the admittance of the resonators, the three terms to the right of equation 3.8 need to be expressed in terms of the electromechanical properties of the resonator. The input electromechanical coupling coefficient is determined by a modal analysis approach described below.

3.3.2.1. Electromechanical coupling

The electromechanical coupling coefficient is a constant representing the piezoelectric efficiency of a piezoelectric material. It represents the efficiency of converting electrical energy (applied across the electrodes of a piezoelectric ceramic) into mechanical energy.

Input Electromechanical Coupling

The electromechanical coupling at the input port, η_1, is a function of the piezoelectric property of ZnO. Using the work function, the modal force F_1 defined at $x=0$ is equated to the applied force from the piezoelectric film F_P which has an effectiveness that is dependant on the strain in the structure $\varepsilon(x)$.

$$W = F_1 \cdot \overline{Z} = \int_{L_{e1}} F_p \varepsilon(x) dx \qquad [3.12]$$

The strain as shown in figure 3.9, in the 1D block resonator model is simply $\overline{Z} \cdot d\phi / dx$, and the applied force from the piezoelectric film is:

$$F_P = \sigma_P A = d_{31} E_1 E_p b(x) h = d_{31} V_1 E_p b(x) \qquad [3.13]$$

Substituting the equation above for the modal force:

$$F_1 = \frac{1}{\overline{Z}} \int_0^L F_P \left(\overline{Z} \frac{d\phi(x)}{dx} \right) dx = \int_{x=0}^{x=L} d_{31} V_1 E_p b_1(x) d\phi(x) \qquad [3.14]$$

$$F_1 = d_{31} V_1 E_p \left[b_1(x) \phi(x) \right]_{x=0}^{x=L} \qquad [3.15]$$

where b_{1i} is the width of the i^{th} input electrode, and x_{ai} and x_{bi} are the defining boundaries of the i^{th} input electrode. Therefore the input electromechanical coupling coefficient η_1 is:

$$\eta_1 = d_{31} E_p \left[b_1(x) \cos\left(\frac{n\pi x}{L} \right) \right]_{x=0}^{x=L} \qquad [3.16]$$

Output Electromechanical Coupling

The electromechanical coupling at the output port is a function of the output charge due to the mechanical excitation of the block. The charge at the output is found by integrating the piezoelectrically-induced charge per unit area, D_3, over the area of the electrode:

$$Q_2 = \int_0^L \int_0^{b_2} D_3 dy dx = \int_0^L \int_0^{b_2} \left(\varepsilon E_3 + d_{31} T_1 \right) dy dx \qquad [3.17]$$

Typically, the sense electrode is maintained at zero DC field ($E_3 = 0$), and the stress is:

$$T_1(x) = E_P S_1(x) = E_P \left(\frac{dZ(x)}{dx} \right) = E_P \overline{Z} \frac{d\phi(x)}{dx} \qquad [3.18]$$

Therefore, the charge at the electrode is:

$$Q_2 = d_{31} E_p \overline{Z} \int_0^L b_2(x) \frac{d\phi(x)}{dx} dx \qquad [3.19]$$

$$Q_2 = d_{31} E_p \overline{Z} \left[b_2(x) \phi(x) \right]_{x=0}^{x=L} \qquad [3.20]$$

where b_{2i} is the width of the i^{th} output electrode, and x_{ai} and x_{bi} are the defining boundaries of the i^{th} output electrode.

The electromechanical coupling η_2 at the output becomes:

$$\eta_2 = d_{31} E_p \left[b_2(x) \cos\left(\frac{n\pi x}{L} \right) \right]_{x=0}^{x=L} \qquad [3.21]$$

3.3.2.2. Mechanical Frequency Response & Mobility

For any 1 Degree of Freedom (DOF) mechanical system the relationship between the vibration amplitude and modal force (defined at the same location) is:

$$\frac{Z(s)}{F(s)} = \frac{1}{m_n s^2 + c_n s + k_n} \quad [3.22]$$

where m_n, c_n, and k_n are the effective modal mass, damping, and stiffness at the point of interest.

For the 1D block resonator, the effective mass can be found by equating the kinetic energy. Conveniently using x=0 for the point of interest, the parameters are:

$$m_n = \rho A \int_L \phi^2(x) dx = \frac{\rho A L}{2} \quad [3.23]$$

$$k_n = \omega_n^2 m_n = \frac{n^2 \pi^2 E A}{2L} \quad [3.24]$$

$$c_n = \frac{m_n \omega_n}{Q} = \frac{n \pi A \sqrt{E \rho}}{2Q} \quad [3.25]$$

Therefore, the mobility of the mechanical resonator is:

$$M(s) = s \frac{Z(s)}{F(s)} = \frac{1}{m_n s + c_n + k_n / s} \quad [3.26]$$

Observing that this expression is identical in form to the admittance of a series RLC, the mobility can be modeled with the following series RLC components:

$$L_n = m_n, \quad C_n = 1/k_n, \quad R_n = c_n$$

3.3.3. Electrode Design

Symmetric Full Length Electrodes

For a resonator with symmetrical electrodes ($b=b_1=b_2$), the input and output electromechanical coupling coefficients are equivalent:

$$\eta = \eta_1 = \eta_2 = d_{31} E_p b(x) \cos\left(\frac{n\pi x}{L}\right)\Bigg|_{x_1}^{x_2}$$

Therefore to maximize η, the electrodes must span across the entire width of the block, ($b=w/2$). Figure 3.8 shows the nodes of the normal strain curve for the 1st three length extensional modes. These are the electrode placement boundaries, x_1 and x_2, to optimize η. For full length electrodes, where $x_1 = 0$, and $x_2 = L$, we obtain the following expression:

$$|\eta| = d_{31} E_p b\left[1 - \cos(n\pi)\right]$$

The electromechanical coupling coefficient $\eta=0$ for even n as expected due to charge cancellation, and $\eta = 2d_{31}E_Pb$ for odd n, regardless of the mode number.

3.3.4. Equivalent Electrical Model

The equivalent circuit for resonating systems has been widely investigated [47, 48]. Adopting the same concepts of network theory, a two-port resonator can be modeled by an admittance matrix **Y** as in figure 3.10.

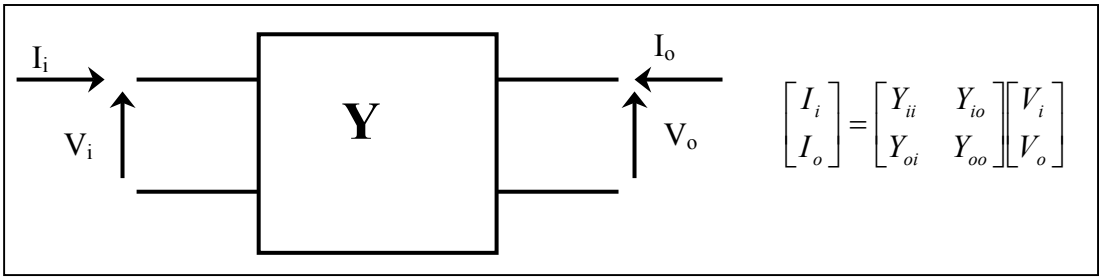

Figure 3.10 Admittance model for a two-port resonator

The admittance matrix describes the resonator in its most general form and allows deriving important information related to both its input and output characteristics. The overall transfer function Y_{21} is given by:

$$Y_{21}(s) = \eta_1(s) \cdot M(s) \cdot \eta_2(s) = \frac{\eta_1 \eta_2}{m_n s + c_n + k_n / s} \qquad [3.28]$$

Figure 3.11 represents the equivalent LCR circuit model for the block resonator where the equivalent series RLC parameters for the admittance Y_{21} are:

$$R_x = \frac{c_n}{\eta_1 \eta_2} = \frac{1}{\eta_1 \eta_2} \frac{n\pi A \sqrt{E\rho}}{2Q} \qquad [3.29]$$

$$L_x = \frac{m_n}{\eta_1 \eta_2} = \frac{1}{\eta_1 \eta_2} \frac{\rho A L}{2} \qquad [3.30]$$

$$C_x = \frac{\eta_1 \eta_2}{k_n} = \eta_1 \eta_2 \frac{2L}{n^2 \pi^2 E A} \qquad [3.31]$$

For full-length symmetrical electrodes, the electro-mechanical coupling coefficient is given by $\eta = 2 d_{31} E_p b$, where b represents the width of the electrode. The capacitors C_{PAD} (drive and sense) model the static capacitance between the electrodes and the device layer. The two transformers in the model account for the isolation between the input and output electrodes. An additional capacitance C_F is placed to model the direct feed-through

between the two ports of the resonators. A large C_F can prevent the output signal to the point where the resonant peak cannot be detected.

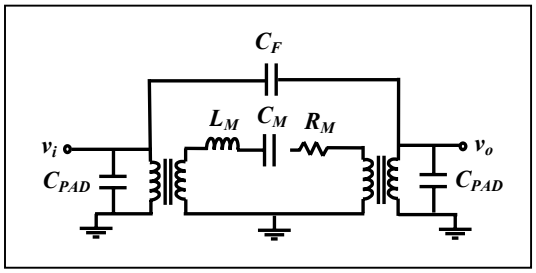

Figure 3.11 Equivalent electrical model of the two-port block resonator

Knowing the equivalent circuit model of these resonators, the design can be optimized for the desired performance measures. Using equation 3.29, the motional resistances for the 1st and 3rd extensional modes of the 120μm×30μm piezo-on-silicon block resonator are calculated to be 9.5kΩ and 15.5kΩ, respectively (using material properties from Table 3.1). The motional resistances of VHF & UHF MEMS resonators (not including FBARs) are typically in the range of a few kΩ to several MΩ.

In order to reduce the motional resistance of a resonator, the input and output electromechanical coupling coefficients should be maximized. We also find that reduction of the device thickness *h* results in a lower motional resistance, simply from the reduction in the mechanical stiffness of the resonator body. However, a compromise between device thickness and motional resistance must be made, since reduction in the thickness of the single crystal silicon resonator body will most likely decrease the quality factor. Increasing the width of the resonator, and subsequently the width of the electrodes, also lowers the motional resistance. It is clear that R_M increases linearly with mode number.

3.3.5. Finite Element Modeling

Finite element modal analysis was performed in ANSYS to aid with the design of the block resonators. The block structure was originally intended to operate in the first and third length-extensional modes as shown in figure. 3.12 a, b. Since the zinc oxide and aluminum layers are relatively thin compared to the resonator body, the 3D model included only the anisotropic SCS block and support tethers. The support tethers are assumed to be perfectly clamped at the ends and are centrally located. The silicon block is tightly meshed with tetrahedral SOLID187 elements. Figures 3.12a, b are contour plots of the displacement in the z direction (normal to the surface) overlaid on the mode shape. They show the first and third length-extensional modes for a 120µm long by 30µm wide centrally-supported silicon block at 35.7MHz and 104MHz, respectively.

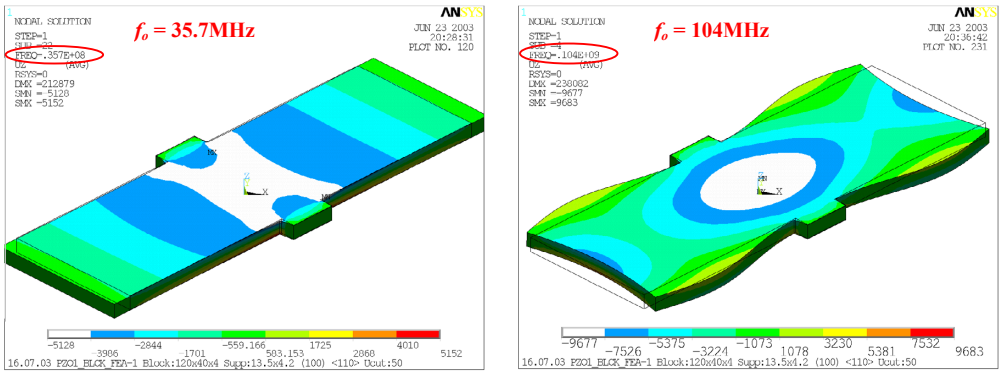

Figure 3.12 ANSYS finite element modal analysis mode plot showing (a) 1st extensional mode and (b) 3rd extensional mode in a 120µm×30µm block

3.3.6. Stress Compensation

The placement of the ZnO film over the SCS device introduces a number of a stresses in the device due to a difference in material properties. Considering a ZnO film on a SCS

substrate such that the layers are unconstrained and stress-free, the electric, thermal and residual stress effect can be given by:

$$\Delta\varepsilon_{piezo} = d_{31}E_3 \quad [3.32]$$

$$\Delta\varepsilon_{thermal} = \Delta\alpha\Delta T \quad [3.33]$$

$$\Delta\varepsilon_{residual} = \Delta\left(\frac{\sigma_r}{E}\right) \quad [3.34]$$

where, $\Delta\alpha$ is the difference in thermal expansion coefficient between the two layers, ΔT the change in temperature, and ε the elastic constant.

The material properties of ZnO and SCS are summarized in Table 3.1.

Table 3.1 ZnO and SCS material properties

Parameter	Symbol	ZnO	SCS
Piezoelectric coefficient	d_{31}	5 x 10^{-12} pC/N [49]	N/A
Thermal coefficient	α	6 x 10^{-6} 1/K [50]	2.33 x 10^{-6} 1/K [51]
Residual stress	σ_r	-100 MPa	0
Elastic Modulus	E	123 GPa [52]	129.5 GPa [52]

The residual stress is minimized by performing a post-deposition anneal of the ZnO film. Due to heat treatment, boundary defects are eliminated and the c-axis preferred orientation of the polycrystalline zinc oxide is improved [53-58].

CHAPTER IV

FABRICATION

4.1. Process Flow

Figure 4.1 shows a brief process flow for the piezoelectrically-transduced SCS resonators. An SOI substrate was used because of the stress-free nature and high mechanical quality factor of SCS.

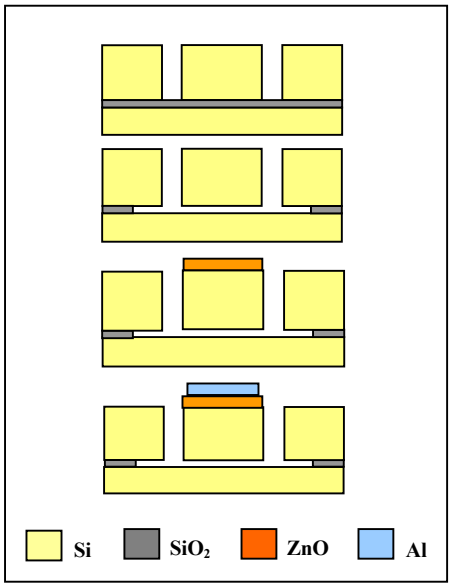

Figure 4.1 Schematic of the process flow

The fabrication process has three masks. The resonator body is defined by etching shallow trenches (4μm wide) into the device layer and landing on the buffer oxide layer of the SOI substrate as seen in figure 4.1. A snapshot of one repeating unit (~ 1.2cm) of the trench mask is shown in figure 4.2. The following recipe [59] was used to etch trenches in the STS ICP system:

Table 4.1 Recipe to etch trenches in the STS ICP system

Passivation time (sec)	Etch time (sec)	Pressure (mTorr)	RF Platten power (watts)	RF Generation power (watts)
3	4	8	25	600

The device layer of the selected SOI is p-type, low resistivity, <100> orientation with a nominal thickness of 4±1μm. The device thickness is defined by the thickness of the device layer. A cavity is opened underneath the beam by isotropic etching of the buffer oxide layer in HF to H_2O in ratio 1:1. The etch rate was approximately 2.3 μm/min. Therefore in the process of releasing the largest device (480 μm x 240 μm), the smaller devices experienced large undercut.

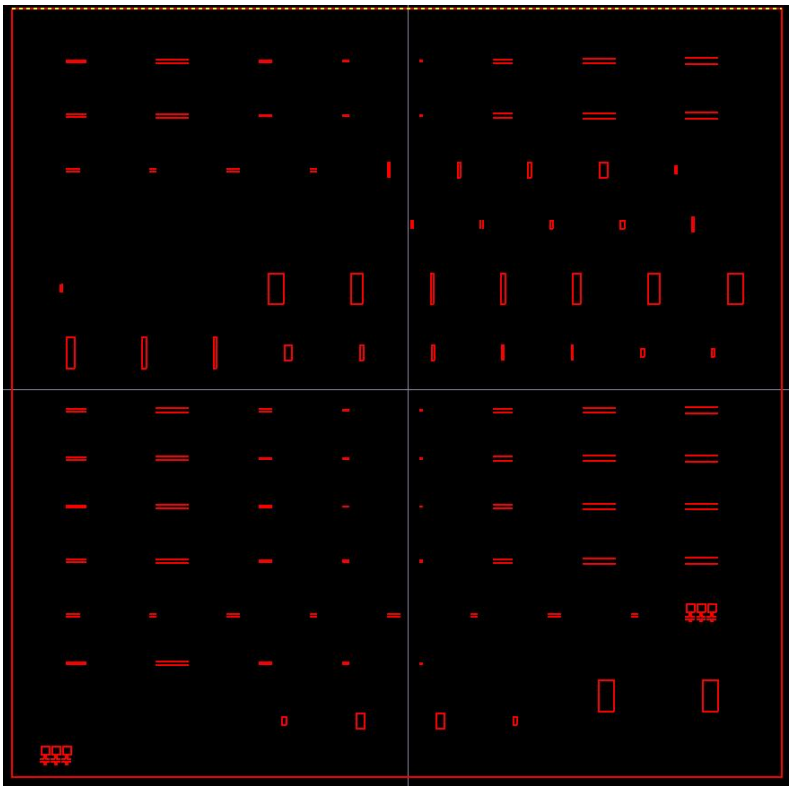

Figure 4.2 Mask 1: Trenches defining resonator body

The active piezoelectric film is sputter-deposited on the silicon substrate using an RF sputter system. ZnO was selected because of its well-known process of fabrication and ease of integration with current microelectronics. The low-temperature fabrication process makes these devices post-CMOS compatible. A temperature of 215ºC for the silicon substrate, a pressure of 6mTorr, an Ar to O_2 mix ratio of 0.5, and a power of 135W were used as deposition parameters. The piezoelectric film has a thickness of 0.35µm and shows strong c-axis orientation, as confirmed by X-ray diffraction analysis (XRD) shown in figure 4.6. ZnO was patterned using the mask shown in figure 4.3 by wet etching in ammonium chloride (NH_4Cl) at a pH of 5 and 50 deg C. NH_4Cl was selected because it has a very slow etch rate (50Å/s) and enables the definition of small features without severe lateral undercut.

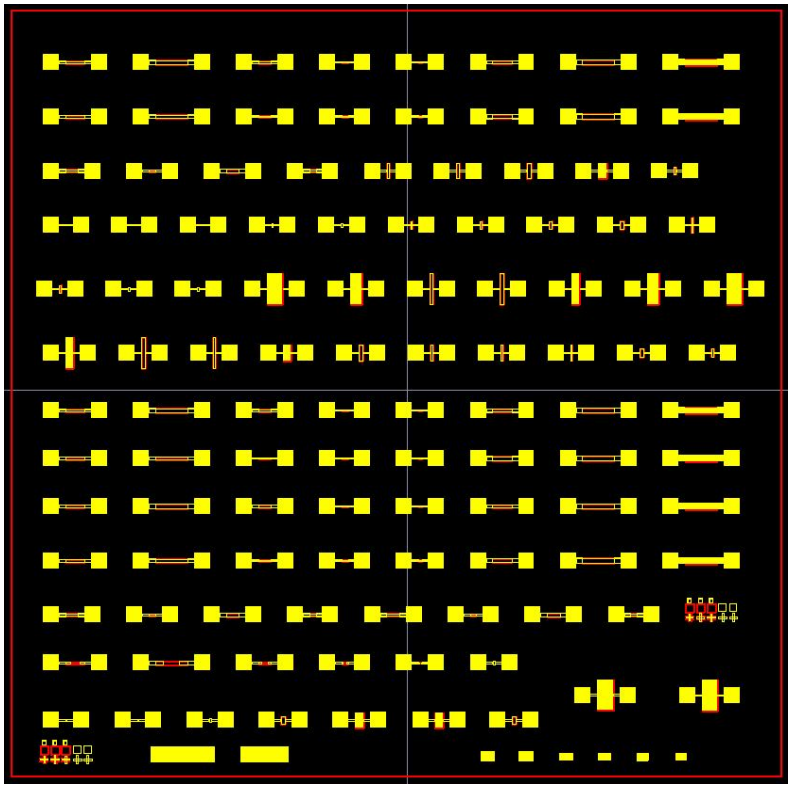

Figure 4.3 Mask 2: ZnO patterning

The aluminum top electrode (1000Å) is defined by the third mask shown in figure 4.4, using lift-off. The thickness of the ZnO and Al layers has been kept small to avoid any detrimental effects on the quality factor and resonance frequency of the resonators due to stacked layers of different materials.

The input and output signal pads are electrically isolated from the silicon substrate by the piezoelectric ZnO film, which exhibits a resistivity value higher than $10^8 \Omega cm$ if an Ar to O_2 mix ratio of 0.5 is used during the deposition phase.

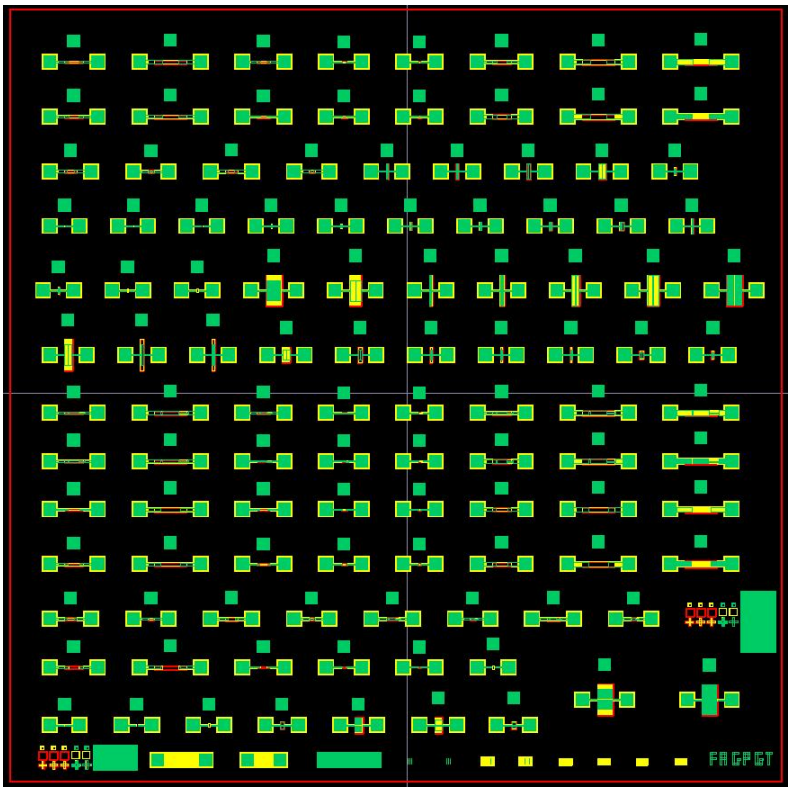

Figure 4.4 Mask 3: Aluminum electrode patterning

4.2. Release Etch Issues

Stiction during the release step is one of the most important problems in MEMS. This phenomenon, due to capillary forces and molecular adhesion, appears during drying after

wet etching. Capillary forces result from trapped liquid that, due to Laplace pressure differences and surface tension forces, produce an attractive force. The presence of the liquid is usually a byproduct of the release process. This capillary force is directly proportional to the surface tension of the last liquid used before drying. The liquid forms a droplet during evaporation between the microstructure and the substrate, and if the drying liquid wets both surfaces, then the droplet has an under-pressure. This results in the collapse of the microstructure if it is not stiff enough. This can often damage devices and promotes the adhesion that results from the Van Der Waals and electrostatic forces.

Solutions to this problem include increasing the stiffness of the microstructure material, or other rinsing procedures such as critical point drying or freeze drying can be used. Put simply, after a device has gone through the sacrificial etch step, it is dried in a fluid that is raised to its supercritical point via high pressure and temp. The result is that, because of the molecular state of the liquid, a meniscus does not form during drying. This was the only approach adopted in this research.

Another alternative is to design special structures on the substrate surface to minimize the area exposed to the liquid. A newer method [60] of dealing with sticking problems is to chemically treat the device surfaces such that they will not stick regardless of contact. For example, it is possible to chemically coat a MEMS device with a very thin monolayer of polymer. Theses chaotic long polymer chains do not exhibit the drastic adhesion problems as crystalline materials.

4.3. Zinc Oxide Deposition

With regards to determining the device performance, the piezoelectric film quality is most critical. All film deposition for these devices has been carried out at the Georgia Tech cleanroom facility. A variety of methods exist for thin film ZnO deposition. Some commonly used techniques are spray pyrolysis [61], pulsed laser deposition [62], chemical vapor deposition [63], molecular beam epitaxy [64], DC sputtering [65] and RF sputtering [66-70].

RF Sputter deposition is the most common technique to obtain piezoelectric ZnO and is the technique used in this research. Extensive characterization of the optimal set of deposition parameters is required to produce a high quality film.

4.3.1. Sputtering system

This process involves high-energy ions that hit the substrate and sputter material from the target onto the substrate. Ar ions are generated in the plasma between the target and the substrate. The target is negatively charged, so the Ar ions impinge the target and not on the substrate which is grounded. Almost all materials can be deposited using sputtering. It provides many parameters for process control. The adhesion of the sputter deposited films is good because of the high kinetic energy with which the sputtered atoms reach the substrate.

The sputtering parameters that can affect quality of the resulting film are RF power, substrate temperature, pressure, O_2 and Ar ratio, and the distance between target and the substrate. Of these the distance is very critical as altering this distance will affect the

number of interactions between the atoms/molecules and the species of the plasma. This also affects the uniformity of the deposited films.

Table 4.2 ZnO deposition parameters for RF Sputter

Fwd RF	Refl RF	O2	Ar	Pressure	Temperature
135 watts	135 watts	20sccm	20sccm	6mTorr	210^0C

4.3.2. X-Ray Diffraction data

XRD is a versatile analytical technique used to analyze crystalline materials. This method of chemical analysis is based on the fact that a given crystalline substance always produces a characteristic diffraction pattern, whether that substance is present in pure state or one constituent of a mixture of substances. The patterns correspond to unique crystal indices which characterize specific substances.

XRD is based on Bragg's law of diffraction, which is schematically represented by figure 4.5 and refers to the simple equation: $n\lambda = 2d \sin\vartheta$, where ϑ is the angle of incidence, d is the distance between atomic layers in a crystal, λ is the wavelength of the incident X-ray beam and n is an integer. It states that if the wavelength of the X-rays going in to the crystal is known, and the angle of the diffracted X-rays coming out of the crystal can be measured, then the spacing between the atomic planes can be determined.

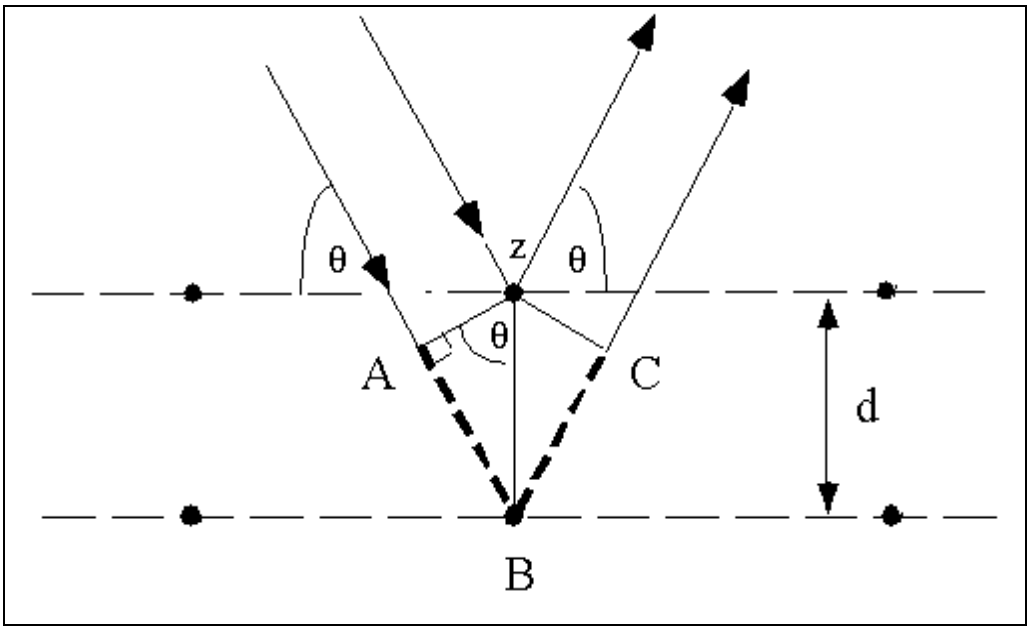

Figure 4.5 Schematic depicting Braggs Law of diffraction

For the piezoelectric ZnO used in this research, orientation along the c-axis, i.e. perpendicular to the substrate, is desired. This can be measured by taking a $\theta - 2\theta$ diffraction measurement of the sample. The x-ray beam was diffracted as the sample was being rotated and a detector recorded the intensity of diffraction. At the end of the measurement, a graph of intensity vs. diffraction angle (2θ) was obtained. Identification was achieved by comparing the x-ray diffraction pattern obtained with an internationally recognized database. Shown below are various XRD measurements from samples with different sputtering parameters. The measurements were all carried out in the Material Science department at Georgia Tech.

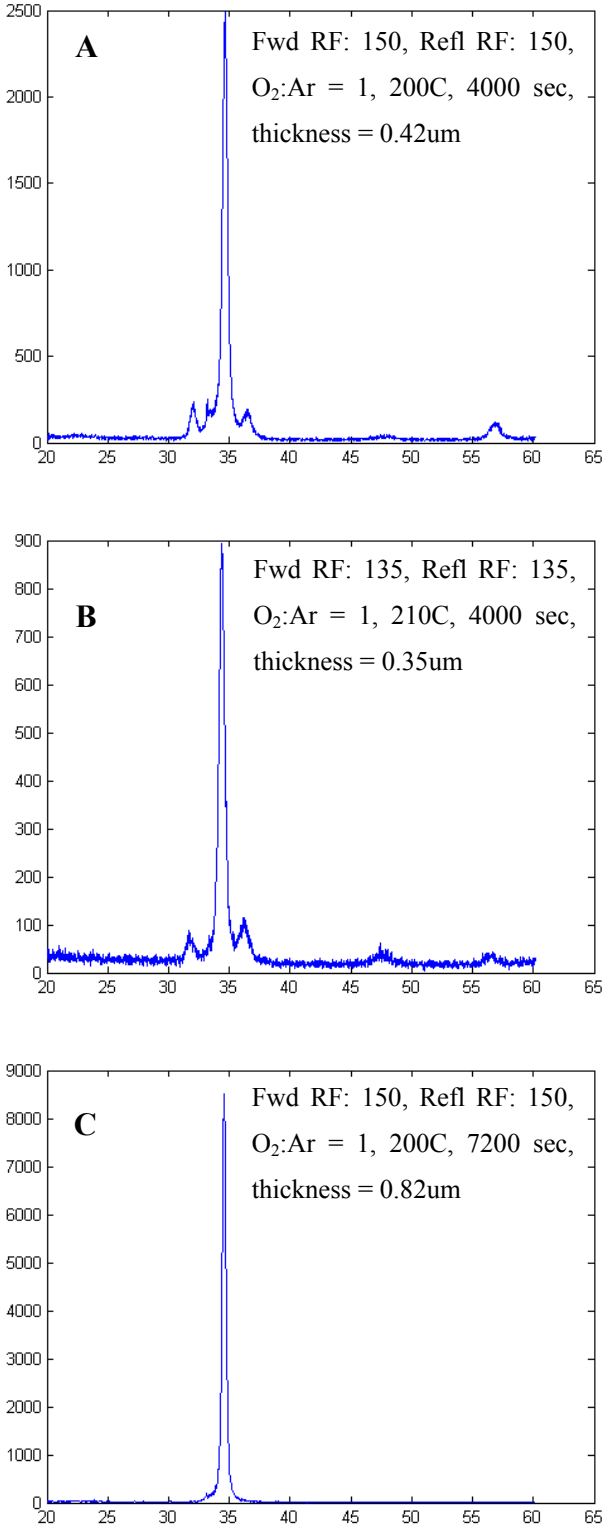

Figure 4.6 XRD plots (A, B, C) of ZnO deposited with different sputtering conditions

Films sputter deposited at 300 watts forward power showed good orientation, i.e. a strong peak at 34^{o} corresponding to the (002) orientation of ZnO, but made the targets prone to cracking at such high power, hence recipes had to be characterized with lower power. Reducing the power from 300 watts to 150 watts will reduce the rate of deposition but still provided good orientation. Varying the temperature from 170 to 230^{o}C it was decided to use 210^{o}C as it resulted in uniform deposition.

It has been shown that gold (Au) would be preferred as a bottom metal to promote oriented growth of ZnO [71, 72]. This was experimented as shown in figure 4.7 for the purpose of introducing a bottom metal layer to act as a bottom electrode for future work to reduce the feed-through capacitance. An additional strong peak was seen close to the desired 002 peak. For perfect (002) orientation, only a strong peak at 34^{o} should be seen. Also Au introduces fabrication complications and hence this was not implemented.

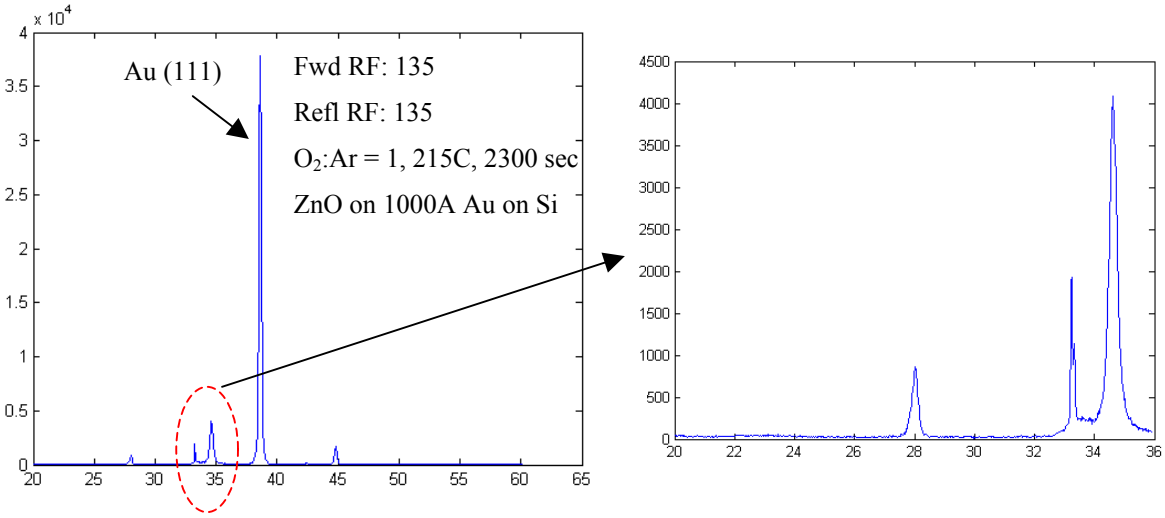

Figure 4.7 XRD plot of ZnO on Au

4.4. New Mask Layout Characterization

A new mask set was designed to incorporate some new disk resonators, more width variations for the blocks and some filter configurations. The trench mask as seen in figure 4.8 was modified to have trenches surrounding the input and output pads to examine support loss. Unfortunately these additional trenches caused problems during the HF release step. In order to release the larger devices of dimensions in the range of 120 to 180 μm the pads suffer from extensive undercut. The dimensions of the pads are 150x150 μm .This leaves a very small amount of oxide that supports the pad in the center and makes that region susceptible to breakage during any stress-inducing processing steps, especially during ZnO deposition.

A separate mask to pattern ZnO was eliminated. This was achieved by using the same mask as that for the electrode patterning. The elimination was aimed at patterning ZnO and the top Al electrodes in one step reducing the amount of processing on the wafer. The patterned Al electrodes could act as an etch mask for the ZnO features. Therefore first an efficient method to pattern the Al electrodes had to be determined.

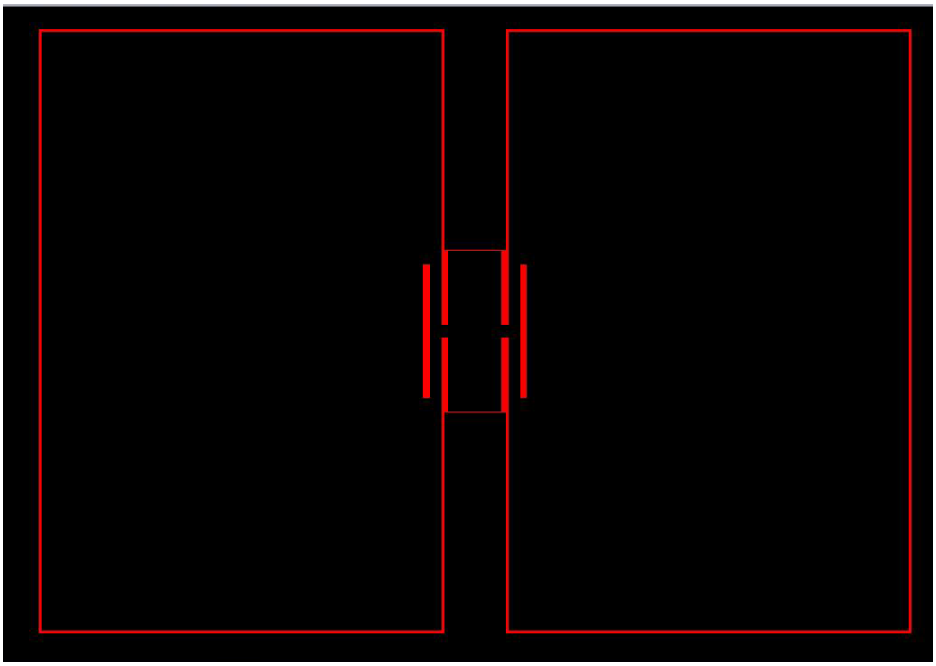

Figure 4.8 New Mask 1: Trenches defining resonator body

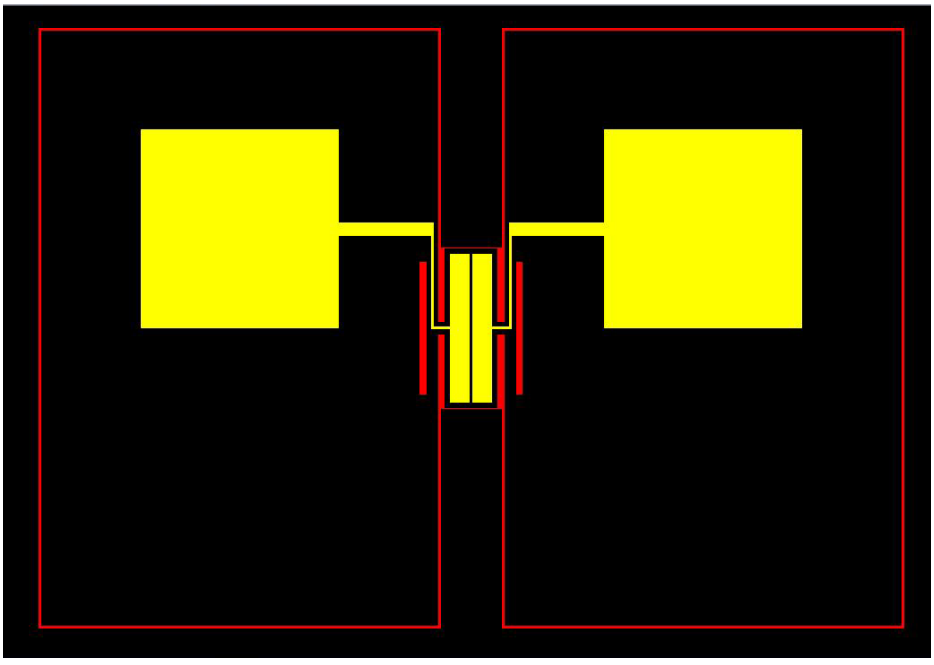

Figure 4.9 New Mask 2: ZnO and Al electrodes patterning

Al electrodes can be patterned a number of ways. The mask was dark data and therefore lift-off was one option with negative resist. NR7-1500 was the negative resist used for the

lift-off. Patterning negative resist is not as simple as working with positive resist. It requires critical pre-baking and post-exposure baking. After several runs, the recipe established for NR7-1500 patterning was the following:

- Spin PR at 3000rpm, 500r/s for 40sec followed by a soft bake at 150C for 60 seconds.
- Expose at 365nm (CI1, intensity set was to 5) for 9 seconds in hard contact mode followed by post exposure bake at 100C for 60seconds.
- Developed in RD6 for 14 seconds

After stripping the PR in acetone, it was noticed that the Al features were curved instead of vertical in many places. This was suspected due to poor adhesion of the PR to the underlying zinc oxide layer. Hence another approach had to be investigated. Dry etch of Al was carried out in RIE with the following recipe:

Table 4.3 Al dry etch recipe in RIE

RF (watts)	DC Bias (volts)	BCl_3 (sccm)	Cl_2 (sccm)	Pressure (mTorr)	Etch rate
100	250	20	5	30	1000A/3min

Al etching in the RIE is load dependant, i.e. the etch rate is inversely proportional to the amount of exposed Al being etched. The issue with this step was the unreliability of the system due to the various materials etched by other users. Now a wet etchant was needed that could pattern Al and not affect the underlying ZnO layer. A mixture of 1gm Potassium Ferricyanide ($K_3Fe(CN)_6$), 1gm Potassium Hydroxide (KOH), and 100ml DI water was used. This wet etchant worked well, providing an etch rate of approximately 665A/min. The lateral undercut was almost negligible. Now that Al was patterned, this

could act as an etch mask to pattern ZnO by either dry or wet etching methods. On wet etching in the NH_4Cl solution, ZnO was heavily undercut and the top Al electrode patterns were peeling off. On dry etching ZnO in the RIE, the gases affected the Al features as well and completely etched away the 1000A thick Al etch mask after 135mins. Therefore this approach of using the Al features as an etch mask for ZnO etch was abandoned, instead it was decided to first pattern ZnO and then repeat the same mask to pattern Al.

Patterning ZnO became a difficult process with the new mask because of the thin traces connecting the pad to the electrodes. The traces loose zinc oxide due to undercut in wet etching of zinc oxide and this renders the device useless. Alternatively dry etching of zinc oxide with 7 μm of photoresist (PR) SPR220 as etch mask was carried out in the Plasma Therm ICP using the recipe in Table 4.4. Dry etching of ZnO has been researched on by some groups [73-75]. This was attempted to carry out a more anisotropic etch of ZnO. PR 1813 and 1827 were also tried as etch mask but their selectivity to the gases used for ZnO etch was too low. The photoresist has to be cured for a minimum of 15 minutes on the hot plate at 125C before dry etch in ICP to ensure the wafer does not get stuck to the mechanical clamp.

Table 4.4 ZnO dry etch recipe in Plasma Therm ICP

RF1 (watts)	RF2 (watts)	CF_4 sccm	H_2 sccm	Pressure	Etch rate A/sec
200	800	50	25	25mTorr	245

One of the biggest problems with this process is the unpredictability of the system. The etch rate varies significantly and also depending on the state of the chamber, the recipe has sometimes even deposited residues back onto the wafer. Another issue is the non-

uniform etch rate across the surface of the wafer. In some areas near the center ZnO does not get completely etched and a longer etch time does not resolve the issue. 589A of thin ZnO film remains in concentric rings around the center of the wafer which makes surface look grainy, and also prevents good contact with device layer in order to ground it.

It was noticed that the PR used as an etch mask was itself undergoing an undercut shown in figure 4.10 that affected the ZnO pattern. This was crucial along the thin traces connecting the pads to the electrodes. PR getting etched completely in this area is shown in figure 4.11.

Dry etch characterization of ZnO was also tried (Table 4.5) in a Reactive Ion Etching (RIE) machine to determine if the PR etch mask had better selectivity.

Table 4.5 ZnO dry etch characterization in RIE

Recipe	Gas1 (sccm)	Gas2 (sccm)	RF (watts)	Initial (A)	Final (A)	Time (min)	Rate (A/min)
1	CF4: 50	H2: 25	300	3500	3300	15	13
2	CF4: 50	H2: 25	375	3300	3200	10	10
3	CF4: 50	H2: 25	400	3200	3000	10	20
4	CF4: 50	H2: 35	400	3000	2900	10	10
5	CHF3: 50	H2: 25	400	3700	3400	20	15

The etch rates were very slow and hence this option was disregarded. Characterization of ZnO patterning is the immediate future direction.

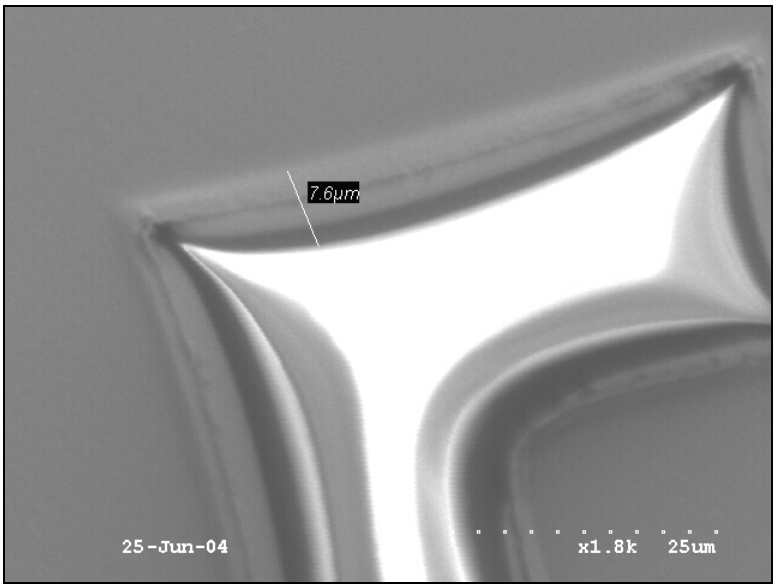

Figure 4.10 PR undercut exposing underlying ZnO during dry etch

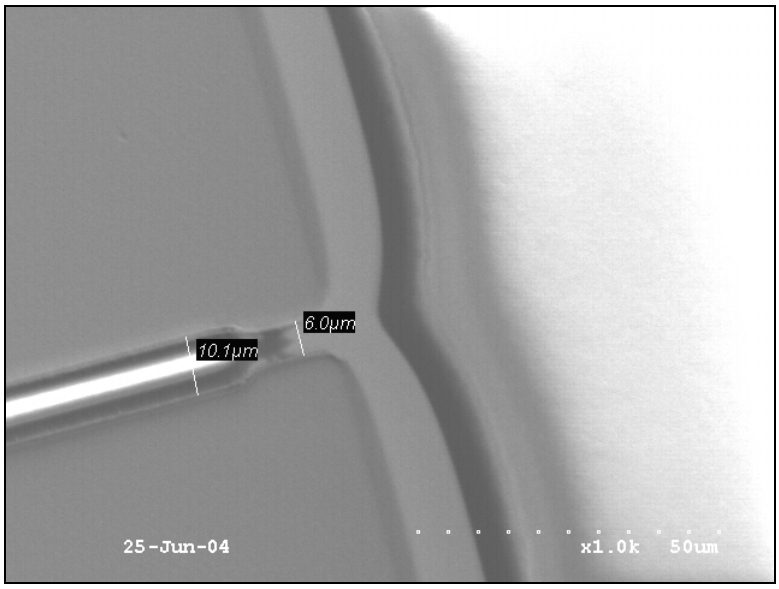

Figure 4.11 PR etched away completely from support junction

The new mask set also had lesser amount of zinc oxide covering the device as compared to the old mask. In most cases maximizing the transducer area is preferred.

CHAPTER V

MEASUREMENT AND CHARACTERIZATION

The fabricated resonators were tested in a custom-built vacuum chamber at 50mTorr. Electrical contact to the resonator was made by wire bonding to the square shaped pads. Each pad has a parasitic capacitance of approximately 10pF to the device layer through the 0.35µm ZnO layer. The device layer was grounded to function as a bottom electrode. The resonator current was detected using a low noise amplifier and no attempt was made to impedance match the resonators to the interface circuitry. The frequency spectra of the resonators were captured using Agilent 4395A network analyzer. In contrast to the capacitive devices, piezoelectric resonators do not require a DC voltage to operate. The testing can also be carried out without the amplifier.

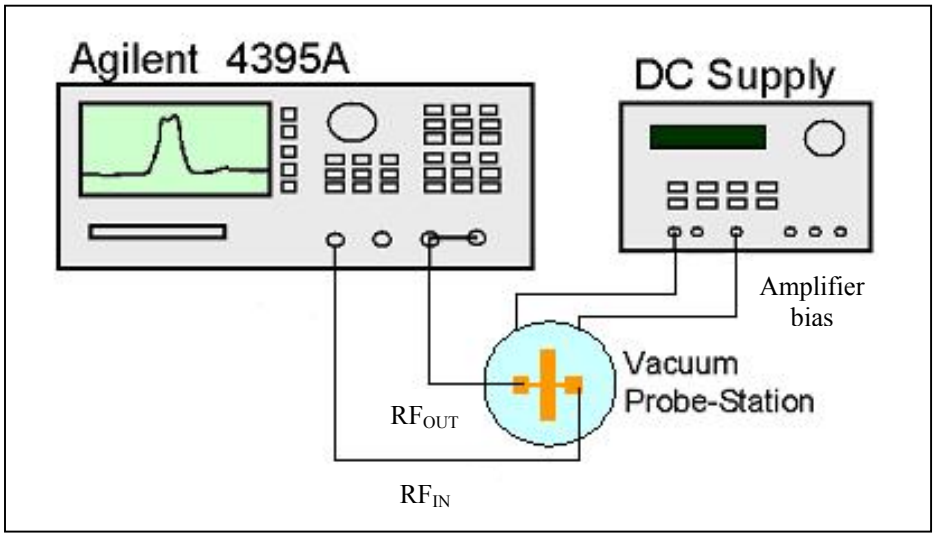

Figure 5.1 Test setup for frequency response measurement

5.1. Frequency Response

Blocks of various dimensions were fabricated. Their calculated longitudinal resonant frequencies have been listed below in table 5.1. It can be seen that by simply reducing the dimension of the block, the high order resonant modes reach the GHz frequency operation range.

Table 5.1 Calculated longitudinal extensional fundamental modes

Length (μm)	1st Mode MHz	3rd Mode MHz	5th Mode MHz	7th Mode MHz
480	9	27	45	63
240	17.2	51.8	86	120.4
120	34.5	104	172.5	241.5
60	69.1	207	345.5	483
40	104	312	520	728
20	207	621	1035	1449

Below are presented frequency responses from the smallest functional device (60um long) till the largest block at 480um.

The smallest device to demonstrate results was a 60x30 μm block. The first fundamental mode was recorded at 68MHz with a Q of ~700. For the same device the third mode was seen at 210MHz with a Q of 12k. This has been the highest Q measured from the results so far. Both frequencies are in close agreement with calculated ones (Table 5.1) as well as with ANSYS plots (71MHz and 213MHz) shown in figure 5.3.

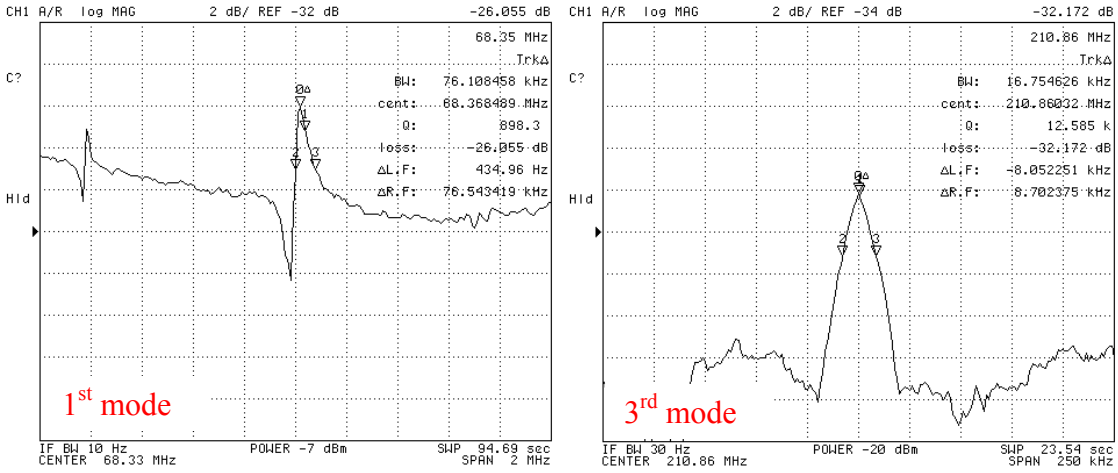

Figure 5.2 First and third extensional modes for a 60x30um block

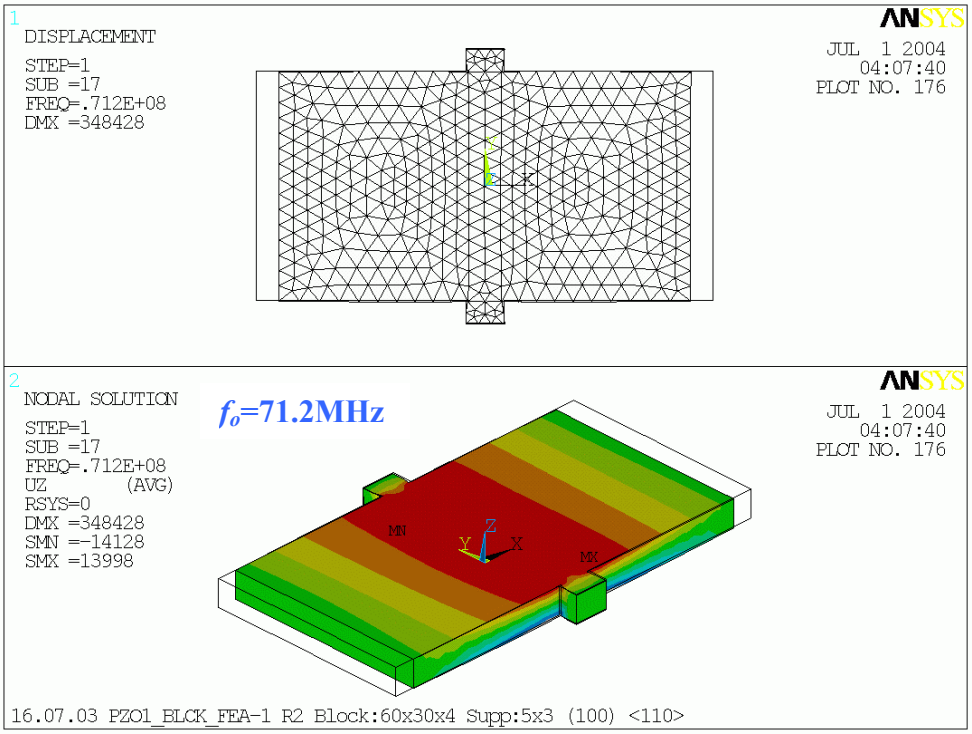

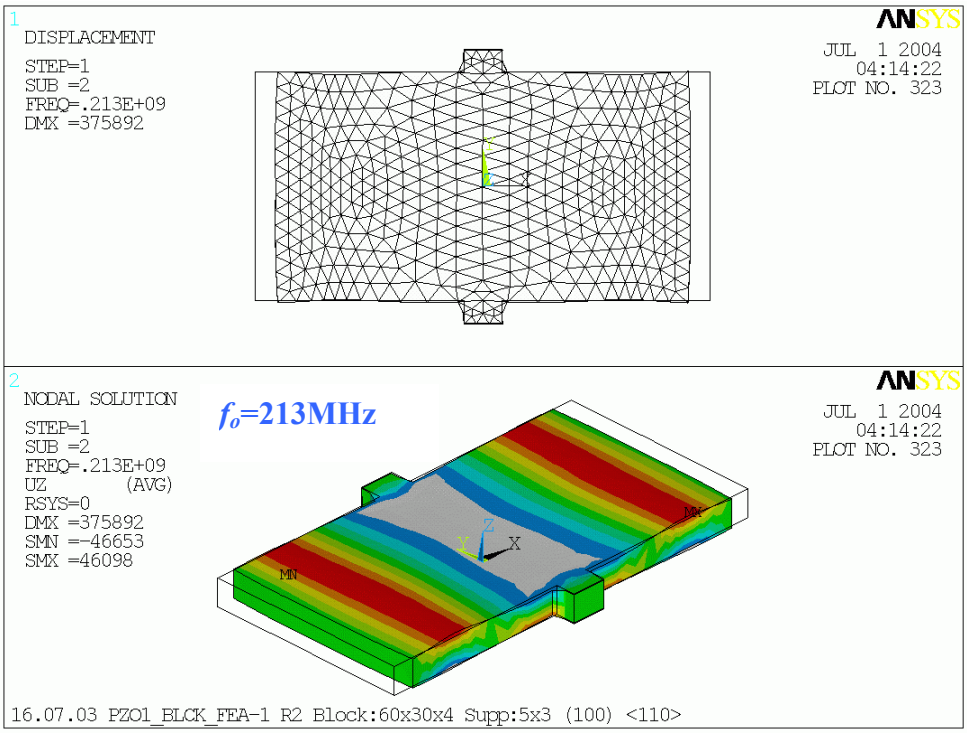

Figure 5.3 ANSYS contour plots of the 1st and 3rd length extensional modes for a 60x30um block

The next dimension was a 120 μm block. Peaks were recorded from blocks of the same length with varying widths of 20, 30 and 40 μm. Shown below are the 1st and 3rd modes again. Different widths show similar frequencies which is as expected, because the extensional mode does not depend on the width of the device.

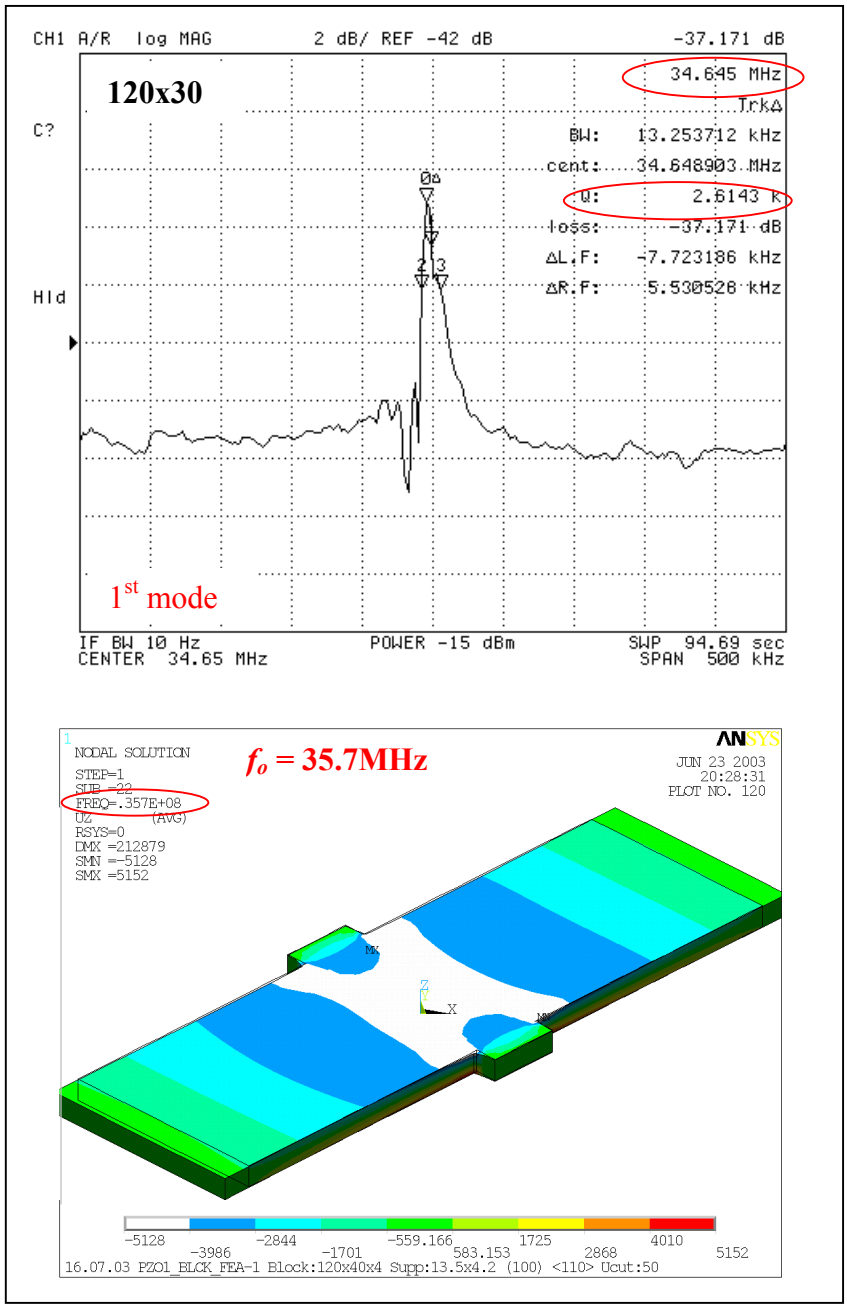

Figure 5.4 Experimental and ANSYS plots for 1st extensional mode of a 120x30um block

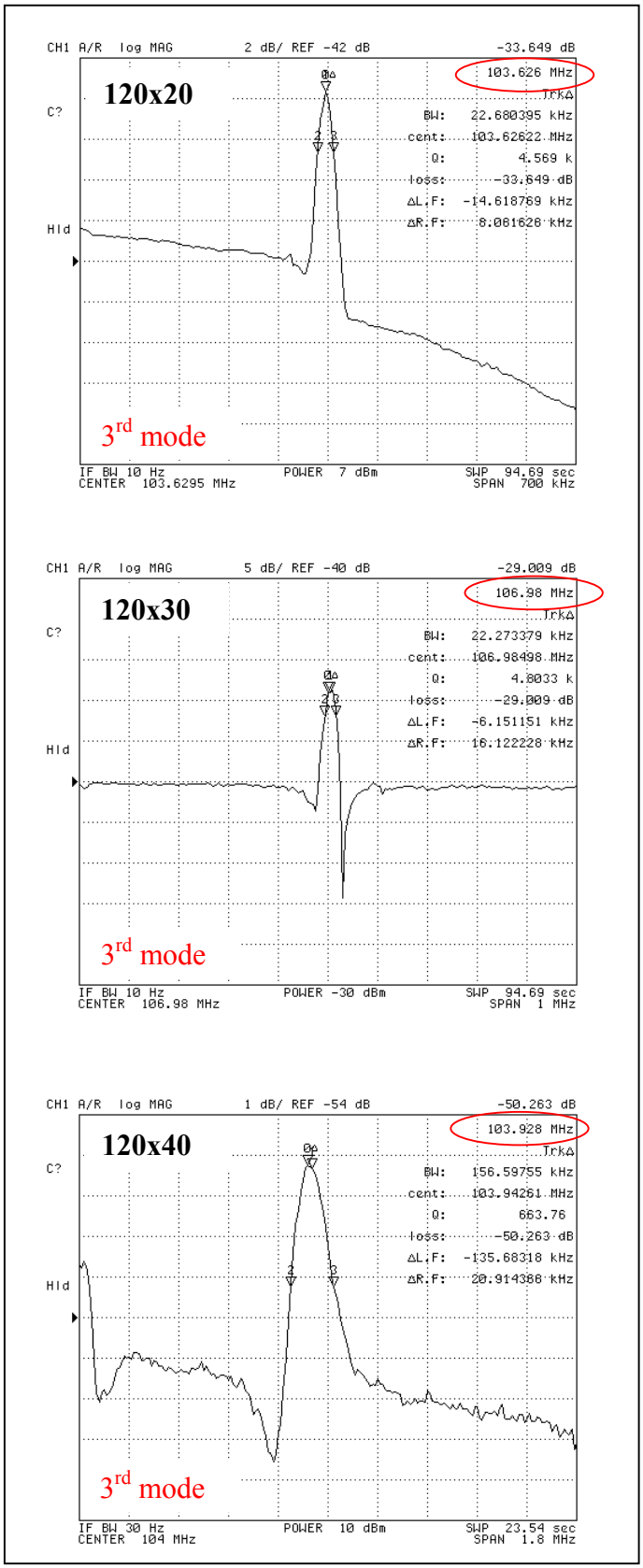

Figure 5.5 Different widths showing the same 3rd extensional mode for a 120um block

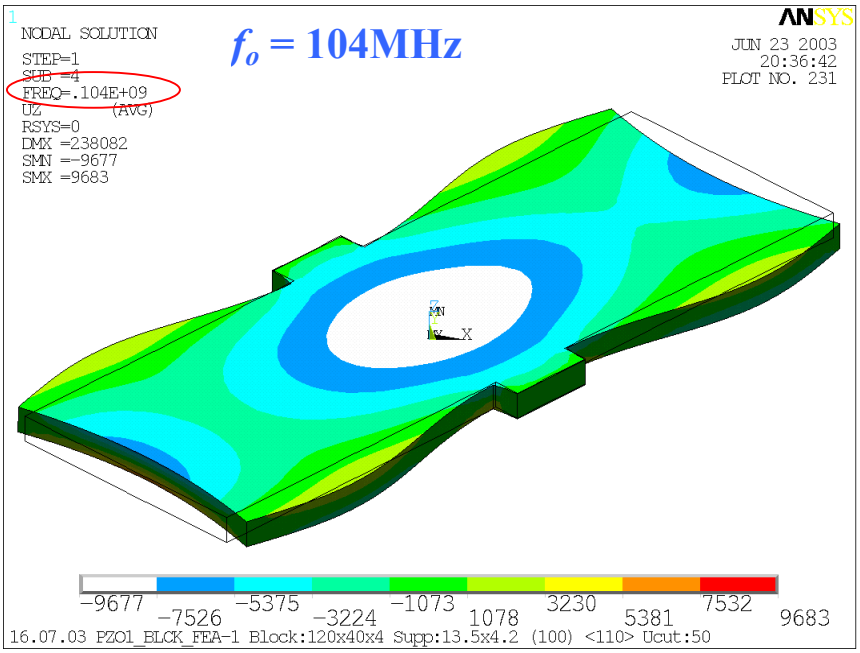

Figure 5.6 ANSYS plot for 3rd extensional mode for a 120um block at 104MHz

The 1st and 3rd extensional modes were also detected for a 240um long block at 17MHz and 49MHz respectively. A relatively high Q of 11k was measured for the 1st mode. The frequency corresponded well with the ANSYS contour plots shown below.

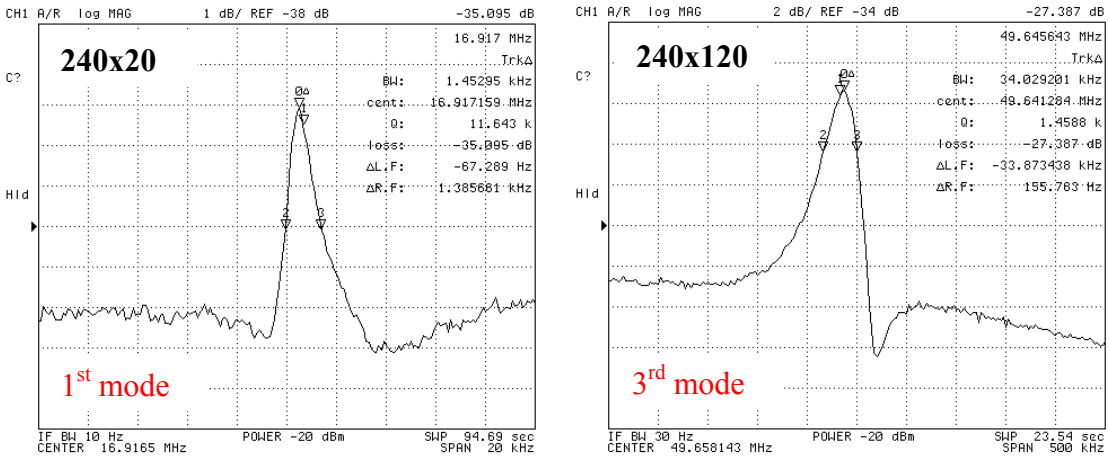

Figure 5.7 First and third extensional modes for a 240um block

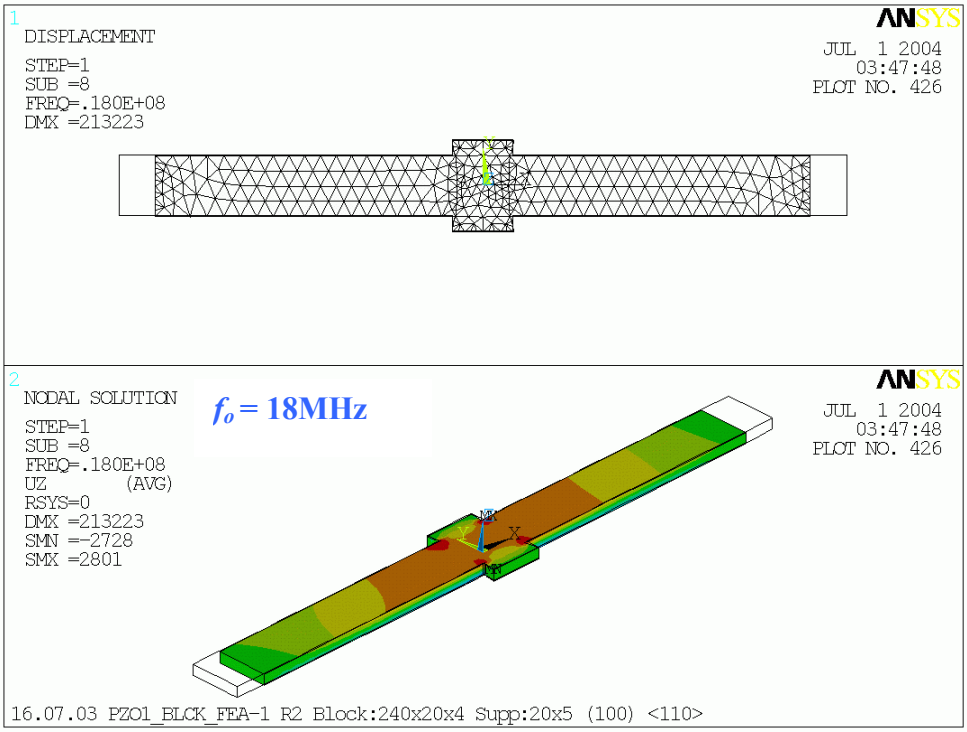

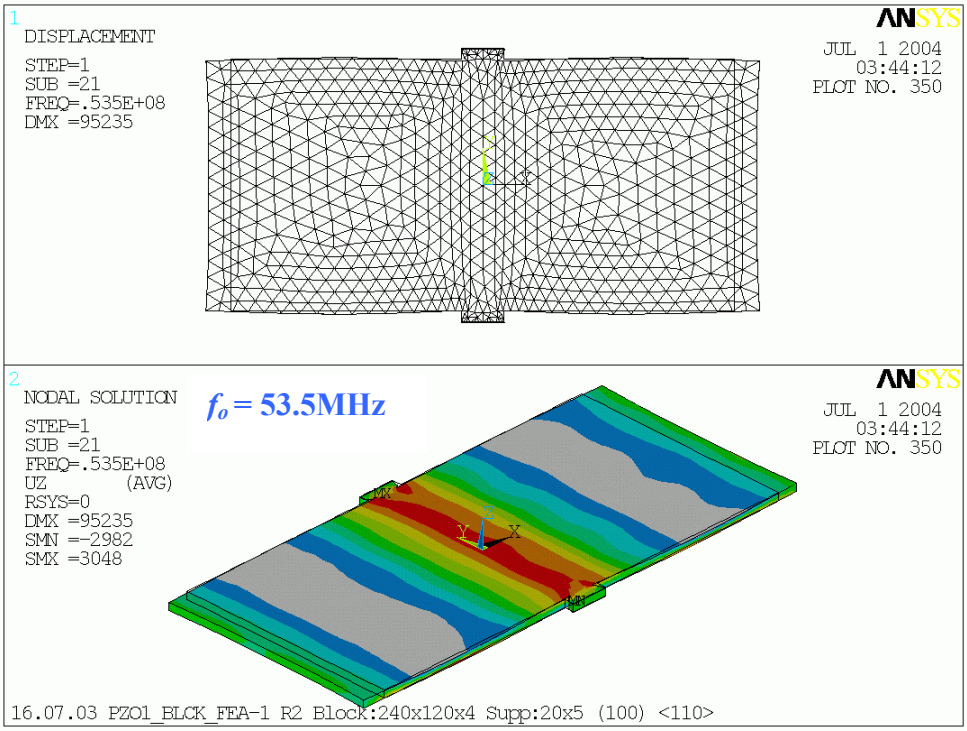

Figure 5.8 ANSYS plots for 1st and 3rd extensional mode for a 240x20um and 240x120um block

Shown in figure 5.9 below is the 1st length extensional mode close to 9MHz for a 480um long block with widths of 60 and 120um. Inconsistent Q values for these peaks can be attributed to process variation across batches and wafers.

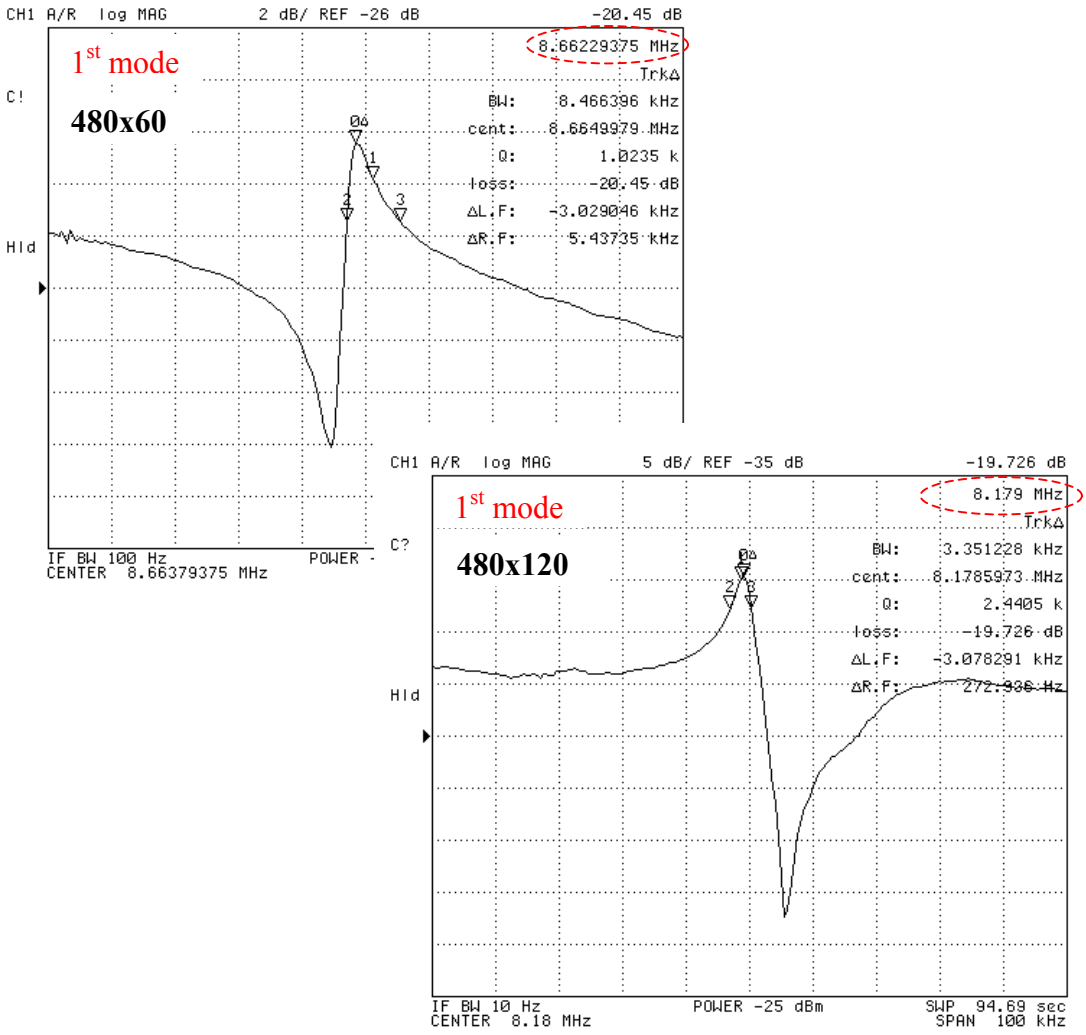

Figure 5.9 Measurement results for the 1st extensional mode for a 480um block with 60um and 120um widths

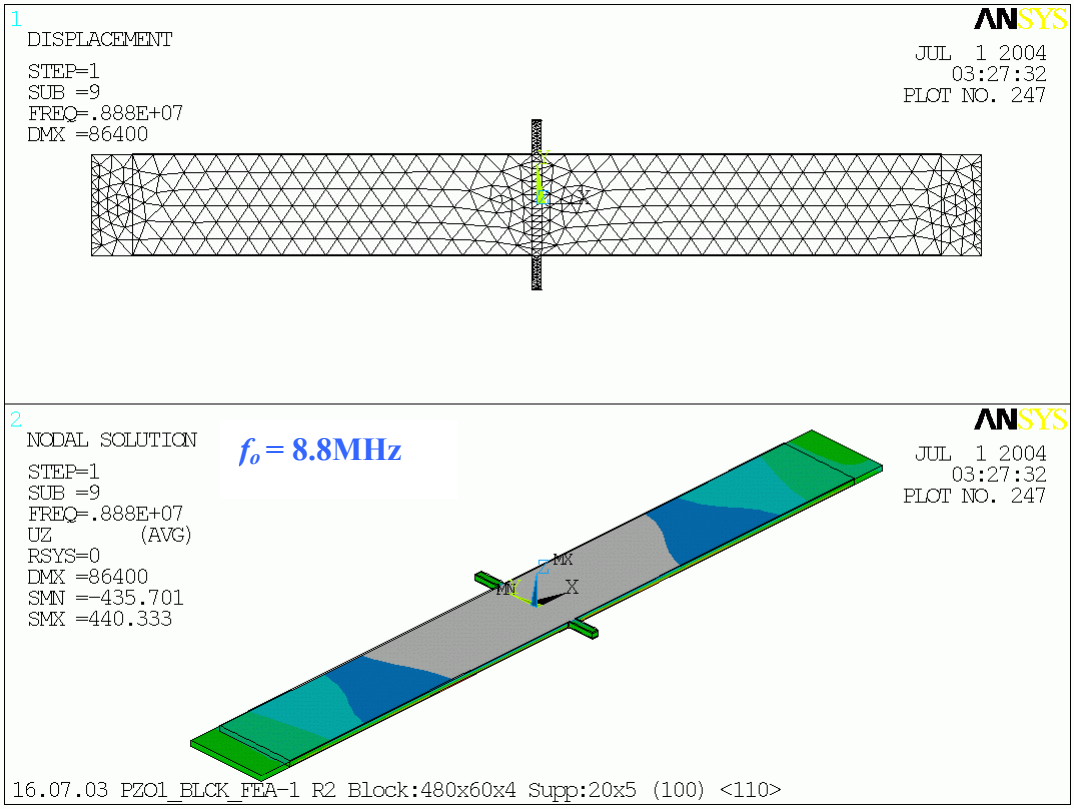

Figure 5.10 ANSYS contour plot for 1st extensional mode of a 408x60um block

An interesting feature of the results recorded for the 480um block was that higher order modes such as the 7th and the 23rd were also seen as shown in figure 5.11 and 5.12. Such higher order modes have not been measured for the other fabricated dimensions. The frequency at the 7th and 23rd modes was approximately 7 and 23 times that of the fundamental mode at 9MHz respectively. This can also be verified by their corresponding ANSYS contour plots shown below. It can be noticed that the 7th mode has 7 regions of alternating compression and extension along the length and similarly the 23rd mode has 23 such regions.

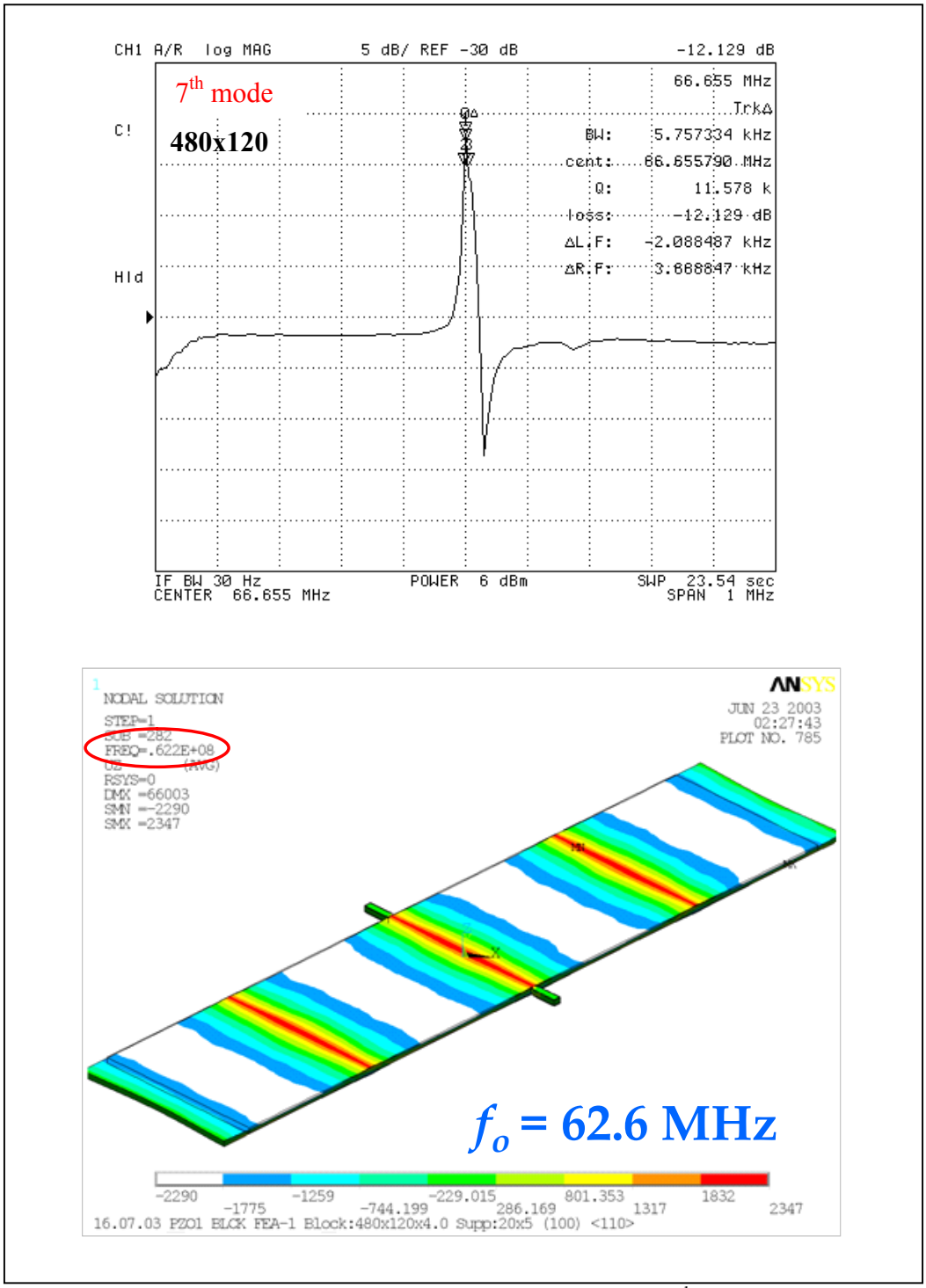

Figure 5.11 Experimental peak and ANSYS contour plot for 7th extensional mode of a 480x120um block

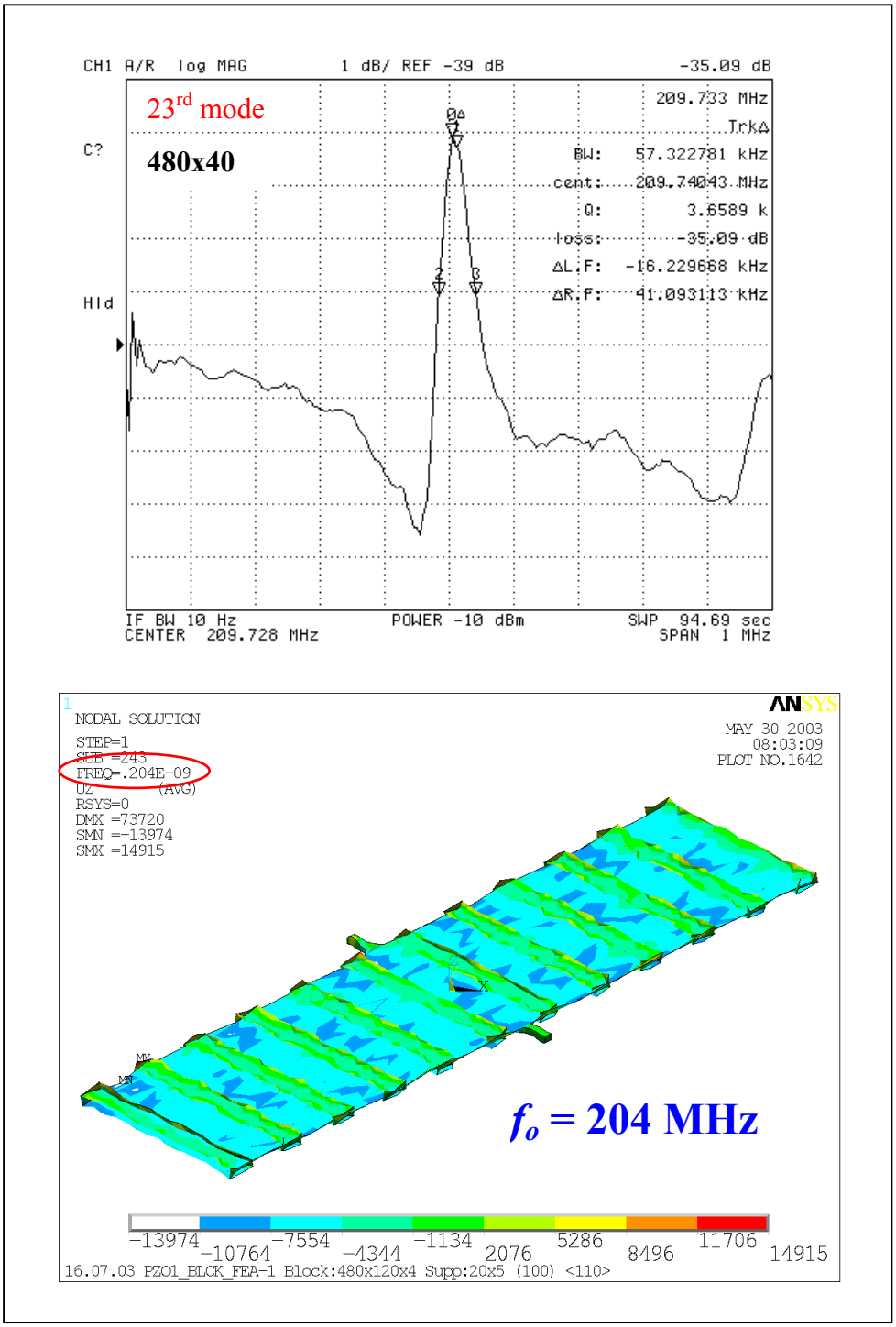

Figure 5.12 Experimental resonant peak for a 480x40um block and ANSYS contour plot for 23rd extensional mode of a 480x120um block

5.2. Temperature Coefficient of Frequency

Figure 5.13 shows the measured temperature characteristic of the 480μm×120μm block resonator operating at the 66.7MHz mode in the range of 20-100^{o}C. The temperature coefficient of frequency (TCF) is linear and measured to be –40ppm/°C. This is mainly caused by the temperature dependence of the Young's modulus of single crystal silicon, reported to be ≈–50ppm/°C [76]. Solely from the temperature dependence of silicon, the expected TCF of these resonators should be ≈–25ppm/°C [77, 78]. The stress relief of ZnO with temperature could further increase the TCF of these resonators.

Table 5.2 Shift in frequency corresponding to change in temperature

Block dimensions	**Temperature in ^{o}C**	**Frequency in MHz**
480x120 2M block	22	66.675
	31	66.65
	36	66.64
	41	66.625
	46	66.61
	50	66.6
	56	66.585
	61	66.57
	65	66.555
	70	66.545
	75	66.53
	80	66.515
	85	66.5
	91	66.485
	96	66.465
	100	66.455

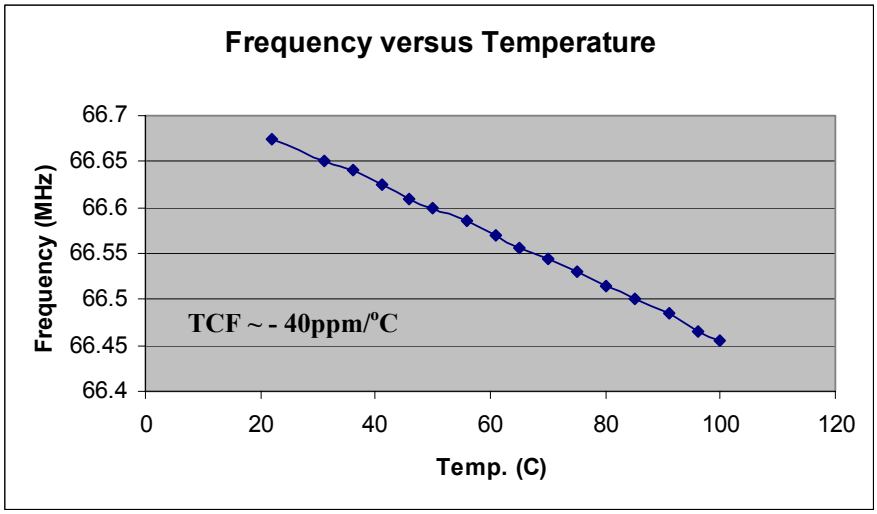

Figure 5.13 Measured TCF for a 480µm×120µm block at 66.7MHz

CHAPTER VI

CONCLUSION AND FUTURE DIRECTIONS

This thesis has shown the use of thin film ZnO for piezoelectric actuation of SCS block resonators in their length extensional modes. Actuation of higher order modes has been demonstrated taking the frequency into VHF. The highest order mode recorded was the 23rd for a 480um long block. Actuating such modes for smaller dimension easily takes the range of operation into UHF making these devices attractive candidates for current demanding RF applications. Their electromechanical coupling has been derived and an equivalent electrical model designed. Test results for various dimensions have been verified using ANSYS.

A fair amount of work remains in fabrication of functional devices with higher resonant frequency and characterization of the piezoelectric response. To better address the stiction problem seen after HF release, dry release is one possible route to investigate. Literature has shown success with release of nano-cantilevers by combining dry release with anti-stiction coatings [79].

To increase the overall performance of the piezo-on-silicon devices, improvements can be made to the electromechanical coupling by considering other piezoelectric materials, such as PZT. Deposition of preferentially oriented ZnO thin-films for piezoelectric actuation has become standard, but the piezoelectric coefficients of ZnO are as much as twenty times smaller than the corresponding piezoelectric coefficients of PZT (Table

6.1). The improved piezoelectric performance that PZT films offer over ZnO films is desired to enhance device performance.

Table 6.1 Piezoelectric coefficient of PZT and ZnO [80]

Material	d_{33}	d_{31}	d_{15}
ZnO	11.67	-5.43	11.34
$Pb(Zr_{.52}Ti_{.48})O_3$	223	-93.5	494

PZT films deposited on silicon form a Pb-rich silicon oxide layer at the interface, with Si diffusing into the PZT film, inhibiting formation of the piezoelectric perovskite phase [81, 82]. Many studies have been conducted to investigate an appropriate bottom metal electrode layer and Pt has been adopted as the standard electrode material for PZT films. It does not oxidize and remains conductive after the PZT deposition process and post-deposition heat treatments [83]. Titanium has been used as an adhesive layer between the Pt bottom electrode and the underlying PZT films primarily because it is known to adhere well to most oxides. The titanium layer also inhibits inter-diffusion between the Si and Pt films, preventing the formation of adhesion killing-platinum silicides [84]. Keeping the electrode/PZT interface in mind along with the inter-diffusion problem between films a schematic of a PZT process flow for future work is shown below in figure 6.1. Alternatively Aluminum Nitride (AlN) can also be used as the piezoelectric layer [85, 86].

Another approach to increase performance is to reduce the feed-through capacitance as well as the pad capacitances. The feed-through can be minimized by introducing a bottom

metal electrode to the process, such as Al that will provide for a better ground plane due to its lower resistivity. Pad capacitances can be reduced by making the pads smaller.

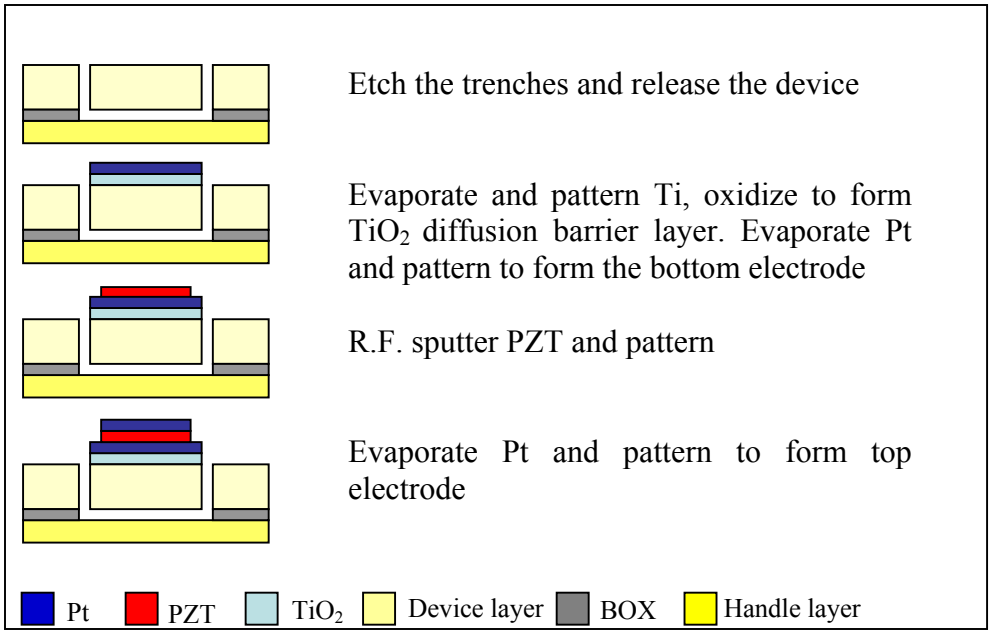

Figure 6.1 Process flow for piezo-on-silicon resonators using PZT

Improvements in the piezoelectric film and reducing the feed-through capacitance hold potential for the piezo-on-silicon devices to become choice candidates for bio-molecule sensing. Detecting mass deposition on the surface of FPW, SAW and QCM resonators has been an application of substantial interest for many years now. Various biological, physical and chemical processes have been characterized. Demonstrated applications include measuring density and viscosity of liquids, quantitative detection of concentration of volatile organic vapors, detecting outputs of a gas chromatographic column, and sensitive and selective detection of biochemically active compounds by employing antibody-antigen, enzyme-substrate and other receptor-protein pairs.

APPENDIX

PROCESS FLOW

Mask 1. SOI TRENCHES

Process step	Process Description	Recipes and Comments
1	Clean wafer	Acetone, Methanol, DI water, dry N_2 gun
2	Dehydration	5 min at 120^{o}C
3	Heat-Bonding	Heat the wafer at 1000C to get rid of any vacuum between oxide and Si layers in the SOI. May help achieve a vertical etch profile of oxide.
4	Spin/bake HMDS and Spin Photo-Resist	Cover 1/3 of the wafer with HMDS: 3000rpm, 500r/s, 15 sec. Bake HMDS 100^{o}C for 30 sec. Cover 2/3 of wafer with 1813: 400rpm, 400r/s, 10 sec. 3000rpm, 500r/s, 30 sec.
5	Soft bake	100^{o}C for 1 min on hotplate
6	Exposure	Using MA-6, CI-2 lamp, vacuum contact, with 20um alignment gap, 150mJ exposure.
7	Develop	MF-319 developer for 1min
8	RIE	Using STS machine to etch 4um of Si
9	HF:H_2O (1:1)	Etch rate ~ 2.3um/min
10	Strip	Microposit remover 1112 at 80^{o}C, followed by Asher to remove any remaining PR residues.

Mask 2. ZnO DEPOSITION

Process step	Process Description	Recipes and Comments
1	Clean wafer	Acetone, Methanol, dry N_2 gun
2	Dehydration	5 min at 120^{o}C
3	ZnO deposition	Using RF sputter, gas ratio: 1:1, Ar: O_2 total flow: 40sccm, deposit 0.4um from a 99.9% ZnO target. Deposition rate: 1000A/hour Pressure: 6mTorr Fwd Power: 135 W Temperature: 210^{o}C

4	Heat to relieve stress	150 ^{o}C for 1 hour
5	Spin/bake HMDS Spin Photo-Resist	Cover 1/3 of the wafer with HMDS: 3000rpm, 500r/s, 15 sec. Bake HMDS 115^{o}C for 30 sec. Cover 2/3 of wafer with SPR1827: 400rpm, 400r/s, 10 sec. 3000rpm, 500r/s, 30 sec.
6	Soft bake	100^{o}C for 2 min on hotplate
7	Exposure	Using MA-6, CI-2 lamp, vacuum contact, with 20um alignment gap, 150mJ exposure.
8	Develop	MF-319 developer for 1min
9	Hard bake	100^{o}C for 15 min on hotplate
10	Wet Etch	Use 5% NH4Cl and 95% H2O at 55-60^{o}C for close to 100 sec. Etch rate: 30A/s. (pH ~ 5)
11	Strip	Microposit remover 1112 at 80^{o}C, followed by Asher to remove any remaining PR residues.

Mask 3. ALUMINUM CONTACT PADS

Process step	**Process Description**	**Recipes and Comments**
1	Clean wafer	Acetone, Methanol, dry N_2 gun
2	Dehydration	5 min at 120^{o}C
3	Spin/bake HMDS and Spin Photo-Resist	Cover 1/3 of the wafer with HMDS: 3000rpm, 500r/s, 15 sec. Bake HMDS 115^{o}C for 30 sec. Cover 2/3 of wafer with SPR220: 400rpm, 400r/s, 10 sec. 3500rpm, 500r/s, 30 sec.
4	Soft bake	115^{o}C for 2 min on hotplate
5	Exposure	Using MA-6, CI-2 lamp, vacuum contact, with 20um alignment gap, 180mJ exposure.
6	Develop	MF-319 developer for 2 min
7	Short BOE dip	To ensure contact of Al to ZnO.
8	Aluminum deposition	Using E-beam deposit 1000A Al.
9	Lift off	Place into hot (80^{o}C) stripper solution, then into ultrasonic bath until Al stops peeling off.
10	Clean	Clean in fresh stripper solution and DI water to rinse off any metallic residues.

REFERENCES

[1] S. No, A. Hashimura, S. Poukamali, F. Ayazi, "Single-crystal silicon HARPSS capacitive resonators with submicron gap-spacing", Solid-State Sensors, Actuator and Microsystems Workshop, pp. 281-284, June, 2002

[2] E. Quandt, A. Ludwig, "Magnetostrictive actuation in microsystems", Sensors and Actuators A, Vol. 81, 2000, pp. 275-280

[3] R. Ruby, et al, "Ultra-miniature High-Q filters and duplexers using FBAR technology", IEEE International Solid-State Circuits Conference, pp. 120-122, 2001

[4] H. Jianqiang, Z. Changchun, L. Junhua, H. Yongning, "Dependence of the resonance frequency of thermally excited microcantilever resonators on temperature", Sensors and Actuators A, Vol. 101, 2002, pp. 37-41

[5] J. Clark, W. Hsu, C Nguyen, "High-Q VHF micromechanical countour-mode disk resonators", IEEE Int. Electron Devices Meeting, pp. 493-496, Dec., 2000

.

[6] S. Bhave, et al, "Poly-SiGe: A High-Q structural material for integrated RF MEMS", Solid-State Sensors, Actuator and Microsystems Workshop, pp. 34-37, June, 2002

[7] R. Mihailovic and N. MacDonald, "Dissipation measurements of vacuum-operated single-crystal silicon microresonator", Sensors and Actuators A, Vol. 50, pp.199-207, September, 1995

[8] J. Cao and C. T.-C. Nguyen, "Drive Amplitude Dependence of Micromechanical Resonator Series Motional Resistance," Digest of Technical Papers, 10th International Conference on Solid-State Sensors and Actuators, Sendai, Japan, June 7-10, 1999, pp. 1826-1829

[9] K. Lakin, "Thin film resonators and filters", IEEE Ultrasonics Symposium, pp. 895-906, 1999

[10] S. Humad, R. Abdolvand, G. K. Ho and F. Ayazi, "High Frequency Micromechanical Piezo-on-Silicon Block Resonators," in Proc. IEEE International Electron Devices Meeting (IEDM'03), Washington DC, Dec. 2003, pp. 957-960

[11] D.L. DeVoe, “Piezoelectric thin film micromechanical beam resonators”, Sensors and Actutators A, Vol. 88, 2001, pp 263-272

[12] E.Zakar, R. Polcawich, M. Dubey, J. Pulskamp, B. Pierarski, J. Conrad, R. Piekarz, “Stress Analysis of SiO_2/Ta/Pt/PZT/Pt Stack for MEMS Application”, IEEE, 2000

[13] B. Piekarski, D. DeVoe, M. Dubey, R. Kaul, J.Conrad, R. Zeto, “Surface Micromachined Piezoelectric Resonant Beam Filters”, Sensors and Actuators, 2000

[14] C. Guyton, Piezoelectricity; an introduction to the theory and applications of electromechanical phenomena in crystals, Dover Publications, New York, 1964

[15] B. Jaffe, W. Cook, H. Jaffe, Piezoelectric Ceramics, Academic Press, New York, NY, 1971

[16] S. Senturia, Microsystem Design, kluwer Academic Publishers, 2001

[17] Z. Wang, Z. Kang, Functional and Smart Materials - Structural Evolution and Structure Analysis, Plenum Press, New York, 1998

[18] M. Vellekoop, C. Visser, P. Sarro, A. Venema, “Compatibility of zinc oxide with silicon IC processing”, Sensors and Actuators, A21-A23, 1027, 1990

[19] G. Sauerbrey, “The use of quartz oscillators for weighing thin layers and for microweighing”, Z. Physics 155, 1959, pp. 206-222

[20] K. Kanazawa, J. Gordon II, “Frequency of a quartz microbalance in contact with a liquid”, Anal. Chem. Vol. 57, 1985, pp. 1770-1771

[21] F. Josse, Z. Shana, D. Radtke, U. Kelkar, D. Haworth, "Analysis of piezoelectric bulk-wave resonators as detectors in viscous conductive liquids", IEEE Trans. Sonics Ultrason., Vol. 37, 1990, pp. 359-367

[22] B. Auld, Acoustic Fields and Waves in Solids, 2nd Edition, Vols. I & II, Krieger Malabar, Florida, USA, 1990

[23] D. Ballantine, R. White, S. Martin, A. Ricco, E. Zellers, G. Frye, H. Wohltjen, Acoustic Wave Sensors, Theory, Design, and Physico-Chemical Applications, Academic Press, San Diego, 1997

[24] R. Schmitt, J. Allen, J. Vetelino, J. Parks, C. Zhang, "Bulk acoustic wave modes in quartz for sensing measurant-induced mechanical and electrical property changes", Sensors and Actuators B, Vol. 76, pp. 95-102, 2001

[25] T. Mattila et all, "A 12 MHz micromechanical bulk acoustic mode oscillator", Sensors and Actuators A, Vol. 101, pp. 1-9, 2002

[26] S. Kim, J. Lee, H. Choi, Y. Lee, "The fabrication of thin-film bulk acoustic wave resonators employing a ZnO/Si composite diaphragm structure", IEEE Electron Device Letters, Vol. 20, No. 3, pp. 113-115, 1999

[27] R. Ruby, P. Merchant, "Micromachined Thin Film Bulk Acoustic Resonators", Proc. IEEE 48th Symposium on Frequency Control, 1994, pp. 135-138

[28] H. Satoh, Y. Ebata, H. Suzuki, C. Narahana, "An Air Gap Type Piezoelectric Composite Resonator", Proc. IEEE 39th Symposium on Frequency Control, 1981, pp. 361-366

[29] S. Krishnaswamy, J. Rosenbaum, S. Horwitz, C. Vale, R. Moore, "Film Bulk Acoustic Wave Resonator Technology", IEEE Ultrasonics Symposium, 1990, pp. 529-536

[30] H. Zhang, E. Kim, "Air-backed Al/ZnO/Al Film Bulk Acoustic Resonator without any support layer", IEEE International Frequency Control Symposium and PDA Exhibition 2002, pp. 20-26

[31] S. Lehtonen et all, “Surface acoustic wave impedance element filters for 5 GHz”, Applied Physics Letters, Vol. 75 No. 1, 1999, pp. 142-144

[32] H. Wohltjen, “Mechanism of operation and design considerations for surface acoustic wave device vapor sensors”, Sensors and Actuators, Vol. 5, pp.307-325, June, 1984

[33] C. Chuang, R. White, J. Bernstein, “A thin-membrane surface-acoustic-wave vapor-sensing device”, IEEE Electron Dev. Lett., Vol. EDL-3, No. 6, pp.145-148, June 1982

[34] S. Martin, K. Schweizer, “Vapor Sensing by Means of a ZnO-on-Si Surface Wave Resonator”, Proc. IEEE Ultrasonics Symposium, pp. 207-212, 1984

[35] J. Grate, M. Klusty, “Surface Acoustic Wave Vapor Sensors Based on Resonator devices”, Anal. Chem., Vol. 63, pp. 1719-1727, 1991

[36] P. Das, C. Lanzl, H. F. Tiersten, “A pressure Sensing Acoustic Wave Resonator”, Proc. IEEE Untrasonics Symp., pp. 306-308, 1976

[37] H. Tiersten, D. Shick, “On the in-plan Acceleration Sensitivity of ST-cut Quartz Surface-Wave Resonators with interior Rectangular Supports”, J. Appl. Phys., Vol. 67, pp. 2554-2566, 1990

[38] S. Martin, G. Frye, “Surface Acoustic Wave Response to Change in Viscoelastic film Properties”, Appl. Phys. Lett., Vol. 57, pp. 1867-1869, 1990

[39] S. Wenzel, R. White, “A multisensor employing an ultrasonic lamb-wave oscillator”, IEEE Trans. Electron. Devices, ED-35, 1988, pp. 735-743

[40] M. Vellekoop, G. Lubking, P. Sarro, A. Venema, “Integrated-circuit-compatible design and technology of acoustic-wave based microsensors”, Sensors and Actuators A, pp. 249–263, 1994

[41] S. Wenzel, R. White, “Flexural plate wave gravimetric chemical sensor”, Sensors and Actuators A, Vol. 21–23, pp. 700–703, 1990

[42] Ph. Luginbuhl et all, “Ultrasonic flexural Lamb-wave actuators based on PZT thin film”, Sensors and Actuators A, Vol. 64, 1998, pp. 41-49

[43] G. Piazza, R. Abdolvand, F. Ayazi, "Voltage-tunable piezoelectrically-transduced single-crystal silicon micromechanical resonators on SOI wafer", Proc. IEEE MEMS‘03, Kyoto, Japan, Jan. 2003, pp. 149-152

[44] G. Piazza, R. Abdolvand, G. K. Ho, F. Ayazi, “Piezoelectrically-Transduced, Capacitively-Tuned, High-Q Single-Crystal Silicon Micromechanical Resonators on SOI Wafers,” Sensors and Actuators A, Vol. 111, Mar 2004, pp. 71-78

[45] William E. Newell, “Electromechanical Tuning Apparatus Particularly for Microelectronic Components”, U. S. Patent No. 3,513,356, May 19, 1970

[46] S.S. Rao, Mechanical Vibrations, 3rd Edition, pp. 512, Addison-Wesley Publishing Company 1995

[47] C.T.-C. Nguyen, “Micromechanical Signal Processors”, Ph.D. Thesis, 1994

[48] M.W. Putty, “Polysilicon Resonant Microstructures”, M.S. Thesis, 1988

[49] H. Cheng, M. T. S. Ewe, R. Bashir, G. C. T. Chiu, “Modeling and control of piezoelectric cantilever beam micro-mirror and micro-laser arrays to reduce image banding in electrophotographic processes”, Journal of Micromechanics and Microengineering, Vol. 11, pp. 1-12, 2001

[50] M. Han, J. Jou, “Determination of the mechanical properties of r.f.-magnetron-sputtered zinc oxide thin films on substrates,” Thin Solid Films, Vol. 2610 (1), pp. 58-64, 1995

[51] A. Cimpoiasu, N. M. van der Pers, Th. H. de Keyser, A. Venema, M. Vellekoop, “Stress control of piezoelectric ZnO films on silicon substrates”.

[52] M. J. Madou, Fundamentals of Microfabrication, 2nd ed., Boca Raton, FL: CRC Press, 2002

[53] R. Lad, P. Funkenbusch, C. Aita, “Postdeposition annealing behavior of rf sputtered ZnO films”, J. Vac. Sci. Tech., Vol. 17(4), pp. 808-811, 1980

[54] F. Hickernell, T. Hickernell, “Stress relaxation in triode sputtered zinc oxide films”, Proc. IEEE Ultrason. Symp., pp. 311–315, 1983

[55] F. Hickernell, “The effect of the structure and composition of zinc oxide films on their elastic properties”, Proc. IEEE Ultrason. Symp., pp. 309–312, 1997

[56] F. Hickernell, “Post-deposition annealing of zinc oxide films”, Proc. IEEE Ultrason. Symp., pp. 489–492, 1981

[57] C. J. Gawlak, C. R. Aita, “Stress relief of basal orientation zinc oxide films by isothermal annealing”, J. Vac. Sci. Technol., Vol. A 1 415–418, 1983

[58] H. Bekman, K. W. Benoist, J. L. Joppe, “Post-deposition annealing of RF-sputtered zinc-oxide films”, Appl. Surf. Sci., Vol. 70/71, pp. 347–350, 1993

[59] S. Pourkamali, F. Ayazi, “Fully single crystal silicon resonators with deep-submicron dry-etched transducer gaps”, MEMS’04, pp. 813-816

[60] R. Maboudian, "Anti-Stiction Coatings for Surface Micromachines," SPIE Vol. 3511, pp. 108-113, 1998

[61] M. de la L. Olvera, A. Maldonado, R. Asomoza, S. Tirando-Gerra, “Characteristics of transparent and conductive undoped ZnO thin films obtained by chemical spray using zinc pentanedionate”, Thin Solid Films, Vol. 411, pp. 198-202, May 2002

[62] T. Nakamura, H. Minoura, H. Muto, “Fabrication of ZnO (0001) epitaxial films on the cubic (111) substrate with C_6 symmetry by pulsed laser ablation”, Thin Solid Films, Vol. 405, pp. 109-116, Feb. 2002

[63] K. Haga, M. Kamidaira, Y. Kashiwaba, T. Sekiguchi, H. Watanabe, “ZnO thin films prepared by remote plasma enhanced CVD method”, J. Cryst. Growth, Vol. 214-215, pp. 77-80, June 2000

[64] K. Nakahara, H. Takasu, P. Fons, K. Iwata, A. Yamada, K. Matsubara, R. Hunger, S. Niki, "Growth and characterization of undoped ZnO films for single crystal based device use by radical source molecular beam epitaxy (RS-MBE)", J. Cryst. Growth, Vol. 227-228, pp. 923-928, July 2001

[65] S. Uthanna, T. K. Subramanyam, B. Srinivasulu Naidu, G. Mohan Rao, "Structure-composition-property dependence in reactive magnetron sputtered ZnO thin films", Opt. Mater., Vol. 19, pp. 461-469, June-July 2002

[66] W. Water and S.-Y. Chu, "Physical and structural properties of ZnO sputtered films", Mater. Lett., Vol. 55, pp. 67-72, July 2002

[67] K. -K. Kim, J. -H. Song, H. -J. Jung, W. -K.Choi, S. -J. Park, J. -H. Song, "The grain size effects on the photoluminescence of ZnO/α-Al_2O_3 grown by radio-frequency magnetron sputtering", J. Appl. Phys., Vol. 87, pp. 3573-3575, April 2000

[68] Y. Yoshino, T. Makino, Y. Katayama, T. Hata, "Optimization of zinc oxide thin film for surface acoustic wave filters by radio frequency sputtering", Vacuum, Vol. 59, pp. 538-545, November-December 2000

[69] K. B. Sundaram and A. Khan, "Characterization and optimization of zinc oxide films by r.f. magnetron sputtering", Thin Solid Films, Vol. 295, pp. 87-91, Feb 1997

[70] S. Takada, "Relation between optical property and crystallinity of ZnO thin films prepared by rf magnetron sputtering", J. Appl. Phys., Vol. 73, pp. 4739-4742, May 1993

[71] Y. Ito, K. Kushida, K. Sugawara, H. Takeuchi, "High-frequency ultrasonic transducer arrays using ZnO thin films", Proc. IEEE Ultrason. Symp., 1993, pp.1117-1125

[72] R. Wagers, G. Kino, P. Galle, D. Winslow, "ZnO acoustic transducers utilizing crystalline gold substrate", Proc. IEEE Ultrason. Symp., 1972, pp. 194-197

[73] H. Kim et all, "Inductively-coupled-plasma reactive ion etching of ZnO using BCl_3 - based plasmas and effect of the plasma treatment on TiyAu ohmic contacts to ZnO", Thin Solid Films, 447 - 448, 2004, pp. 90-94

[74] J. Bae et all, "High-Rate Dry Etching of ZnO in $BCl_3/CH_4/H_2$ Plasmas", Jpn. J. Appl. Phys., Vol. 42, 2003, pp. L535-L537

[75] J. Lee et all, "Dry Etching of ZnO Using an Inductively Coupled Plasma", Journal of The Electrochemical Society, Vol.148 (1), 2001, pp. G1-G3

[76] H. J. Mcskimin, "Measurement of elastic constants at low temperature by means of ultrasonic waves data for silicon and germanium single crystals and for fused silica", Journal of Applied Physics, vol. 24, 1953, pp. 988-997.

[77] J. Hao, S. Pourkamali, and F. Ayazi, "VHF Single Crystal Silicon Capacitive Elliptic Bulk-Mode Disk Resonators Part I: Design and Modeling", *to appear in JMEMS 2004*

[78] S. Pourkamali, J. Hao, and F. Ayazi, "VHF Single Crystal Silicon Capacitive Elliptic Bulk-Mode Disk Resonators Part II: Implementation and Characterization", *to appear in JMEMS 2004*

[79] E. Forsen et all, "Dry release of suspended nanostructures", Microelectronic Engineering, 73-74, 2004, pp. 487-490

[80] C. F. Knollenberg, "Sputter Deposition of Piezoelectric Lead Zirconate Titanate Thin Films for Use in MEMS Sensors and Actuators", M.S. Thesis, UCB 2001

[81] Y. Shichi, S. Tanimoto, T. Goto, K. Kuroiwa, and T. Tarui, "Interaction of $PbTiO_3$ with Si Substrate," Japanese Journal of Applied Physics, Vol. 33, 1994, pp. 5172-5177

[82] L. D. Madsen, and L. Weaver, "Examination of Barrier Layers for Lead Zirconate Titanate Thin Films," Journal of Electronic Materials, Vol. 21, No. 1, 1992, pp. 93-97

[83] P. Muralt et all, "Texture control of $PbTiO_3$ and $Pb(Zr,Ti)O_3$ thin films with TiO_2 seeding." Journal of Applied Physics, Vol. 83, No. 7, April 1998, pp. 3835-3841

[84] G.R. Fox, S. Trolier-McKinstry, S.B. Krupanidhi, “Pt/Ti/SiO_2/Si substrates” Journal of Materials Research, Vol. 10, No. 6, June 1995, 1508-1515

[85] G. Piazza and A. P. Pisano, “Dry-released Post-CMOS compatible contour-mode aluminum nitride micromechanical resonators for VHF applications”, Solid-State Sensor, Actuator and Microsystems Workshop, Hilton Head Island, South Carolina, June 6-10, 2004, pp. 37-40

[86] D. J. D. Carter, J. Kang, D. White, A. E. Duwel, “Fabrication and measurement of an IC-compatible GHz-range piezoelectric longitudinal bar resonator”, Solid-State Sensor, Actuator and Microsystems Workshop, Hilton Head Island, South Carolina, June 6-10, 2004, pp. 254-257